

Fault-tolerant quantum simulation of generalized Hubbard models

Andreas Juul Bay-Smidt,^{1,2,*} Frederik Ravn Klausen,^{1,3} Christoph Sünderhauf,⁴ Róbert Izsák,⁴ Gemma C. Solomon,^{1,2,†} and Nick S. Blunt^{4,‡}

¹*NNF Quantum Computing Programme, Niels Bohr Institute, University of Copenhagen, Denmark*

²*Nano-Science Center and Department of Chemistry, University of Copenhagen, Denmark*

³*Princeton University, Department of Mathematics, Fine Hall*

⁴*Riverlane, Cambridge, CB2 3BZ, UK*

(Dated: January 20, 2025)

Quantum simulations of strongly interacting fermionic systems, such as those described by the Hubbard model, are promising candidates for useful early fault-tolerant quantum computing applications. This paper presents Tile Trotterization, a generalization of plaquette Trotterization (PLAQ), which allows simulation of Hubbard models on arbitrary lattices and provides a framework that enables the simulation of more complex models, including the extended Hubbard model and the PPP model. We consider applications of Tile Trotterization to simulate Hubbard models on hexagonal lattice fragments and periodic hexagonal lattices, analyze gate costs, and provide commutator bounds for evaluating Trotter errors, including new commutator bounds for the extended Hubbard model. We compare the resource requirements of Tile Trotterization for performing quantum phase estimation to a qubitization-based approach, which we optimize for the hexagonal lattice Hubbard model, and demonstrate that Tile Trotterization scales more efficiently with system size. These advancements significantly broaden the potential applications of early fault-tolerant quantum computers to models of practical interest in materials research and organic chemistry.

I. INTRODUCTION

Simulating quantum systems of interacting electrons is an important and complex challenge in the study of molecules and materials. Quantum simulation of fermionic systems is considered one of the most promising applications of quantum computers [1–3], which has motivated resource estimates for quantum simulation of complex systems such as the FeMoco-complex and the cytochrome P450 enzyme [4–6]. Such studies have investigated the electronic structure problem in both first and second quantization, using Gaussian, plane wave or Bloch basis sets [6–12]. Despite significant advances in recent years, general electronic structure simulations of practically relevant and classically intractable systems are estimated to require millions of physical qubits and at least billions of T gates [5, 6], which is far beyond the capabilities of today’s quantum hardware.

Recently, quantum simulations of the Hubbard model [13] have received increased attention due to the model’s relatively low resource requirements, making it a promising candidate for early demonstrations of practical quantum advantage [14–16]. The Hubbard model is a model of interacting electrons which, despite its simplicity compared with the full electronic structure Hamiltonian, is able to describe important aspects of the physics of real materials, and has long been considered a potential model for high-temperature superconductivity [17–19].

Two recent papers by Kivlichan *et al.* [20] and Campbell [21] introduce efficient Trotterization schemes

[22–24] to implement time evolution for the Hubbard model. Hamiltonian time evolution allows for the calculation of dynamical observables such as Green’s functions, which are used to access important quantities including the many-body density of states and spectral functions. Time evolution is also an important subroutine in quantum phase estimation (QPE) [25–28], statistical phase estimation (SPE) [29–33], and in other ground state [34, 35] and Gibbs state [36] sampling methods. QPE can also be performed using the more modern qubitization framework [37–39], which has also been developed for the Hubbard model [40]. These prior studies focus on the square lattice Hubbard model [20, 21, 40] and exclude a broader range of lattices and more complicated electronic interaction models. Very recently, Ref. [41] introduced an extension to the square lattice Trotter scheme in Ref. [21], allowing for beyond-nearest-neighbor hopping terms and multi-orbital interactions.

Extending these simulation methods to other lattices enables the simulation of a broader range of real-life materials with complex electronic behavior. This is especially relevant for lattices that introduce frustration, such as the Kagome and triangular lattices, which are challenging to simulate classically and may provide valuable insights into exotic phases of matter [42, 43]. Including more complicated electronic interaction models allows for studying the effects of non-local electron-electron interactions on charge density waves, charge order and alternative types of superconductivity [44–48]. Conjugated hydrocarbon molecules can also be described by the Hubbard model [49, 50] or more complex extensions such as the extended Hubbard model [51–53] or the PPP model [54–56]. The electronic structure of nanographene is especially interesting because it exhibits topological frustration and strong correlations leading to unconven-

* andreas.bay-smidt@nbi.ku.dk

† gsolomon@chem.ku.dk

‡ nick.blunt@riverlane.com

tional magnetic properties [57, 58]. The PPP model more closely resembles the electronic structure Hamiltonian, and is able to provide insights into electronic states of conjugated hydrocarbons, and can describe charge separated states that are not captured by simpler Hubbard models [56, 59].

In this study, we introduce Tile Trotterization to extend the applicability of PLAQ (developed by Campbell in [21]) to arbitrary lattice Hubbard models, and introduce strategies for simulating more complex Hubbard model variants, including the extended Hubbard model and the PPP model. Tile Trotterization generalizes using plaquettes as the components spanning the square lattice to components of other shapes (called tiles), that can be used to cover any lattice with nearest-neighbor hopping interactions to create efficient Trotter decompositions. We also provide examples demonstrating how Tile Trotterization can be used to simulate various hexagonal lattice Hubbard models, including per-Trotter-step gate costs and Trotter error norms.

One of the main challenges in extending Tile Trotterization to more complicated models while preserving the efficiency of the method is providing tight bounds on the Trotter error. In this work, we prove two commutator bounds for the extended Hubbard model on lattices where all sites have k nearest neighbors in Eqs. (32) and (36), which are used to evaluate the Trotter error norm. The strategy used to evaluate the commutator bounds also provides a framework for evaluating commutator bounds for Hubbard models with longer range interactions.

We further analyze the performance of Tile Trotterization by comparing it to a qubitization-based approach. Trotterization and qubitization have different dependencies on system size and simulation accuracy, leading to interesting trade-offs when comparing their performance for specific applications [60]. We construct qubitized quantum walk operators that are optimized for the Hubbard model on the periodic hexagonal lattice, building upon previous work by Babbush *et al.* in [40]. We provide further optimizations that reduce the cost of the qubitized quantum walk operators and present a detailed analysis of gate and qubit costs. To compare the Trotterization and qubitization approaches, we consider the task of energy estimation by QPE for the periodic hexagonal lattice Hubbard model. We obtain $\mathcal{O}(N^{3/2}\epsilon^{-3/2})$ T-complexity for implementing QPE using Tile Trotterization, compared to $\mathcal{O}(N^2\epsilon^{-1})$ for qubitized QPE, where N is the number of lattice sites and ϵ is the target accuracy. Contrary to common belief that qubitization generally is asymptotically more efficient than Trotterization, we find that Tile Trotterization scales better when ϵ is either constant or allowed to scale with the system size.

Overall, we find that Tile Trotterization implementations of QPE for the Hubbard model and the extended Hubbard model can be performed with T gate costs in the range 10^6 – 10^7 for classically non-trivial system sizes, making Tile Trotterization based quantum algorithms

promising candidates for early fault-tolerant quantum computing applications.

The paper is structured as follows: In Section II we define the generalized Hubbard model, including the standard Hubbard model and the extended Hubbard model used throughout this paper. Section III introduces Tile Trotterization while Section IV presents applications of Tile Trotterization for simulating hexagonal lattice extended Hubbard models. In Section V we present resource estimates for the qubitized quantum walk operator for the hexagonal Hubbard model. Finally, Section VI presents a QPE resource comparison of the simulation methods and models discussed in this paper.

II. HUBBARD MODEL HAMILTONIANS

We consider generalized Hubbard models of the form

$$H = H_h + H_C, \quad (1)$$

with hopping terms given by

$$H_h = -\tau \sum_{i,j,\sigma} R_{ij} a_{i\sigma}^\dagger a_{j\sigma}, \quad (2)$$

where τ represents the hopping parameter. Here, R_{ij} is the adjacency matrix of the lattice with $R_{ij} = 1$ if i and j are neighbors and $R_{ij} = 0$ otherwise. The operators $a_{i\sigma}^\dagger$ and $a_{i\sigma}$ are fermionic creation and annihilation operators acting on a spin- σ orbital at lattice site i . The potential energy, or Coulomb (C), terms have the form

$$H_C = \sum_{i=1}^N U_i n_{i\uparrow} n_{i\downarrow} + \sum_{i \neq j} \sum_{\sigma, \sigma'} C_{i\sigma, j\sigma'} n_{i\sigma} n_{j\sigma'}, \quad (3)$$

where U_i is the on-site interaction strength on site i and $C_{i\sigma, j\sigma'}$ is the interaction strength between electrons in spin orbitals $i\sigma$ and $j\sigma'$ on different sites. The number operator, $n_{i\sigma}$, is defined as $n_{i\sigma} = a_{i\sigma}^\dagger a_{i\sigma}$. The form of H_C varies across the Hamiltonians considered in this paper.

In all systems and models discussed throughout, we represent the number of lattice sites as N and assign two spin orbitals, $\sigma \in \{\uparrow, \downarrow\}$, to each lattice site, such that the total number of spin orbitals is $2N$.

A. The Hubbard Model

First, we introduce the standard Hubbard model, or simply the Hubbard model, with Coulomb interactions between electrons of opposite spin on the same lattice site. The Hubbard model is defined as

$$H_H = H_h + H_I, \quad (4)$$

with potential energy term given by

$$H_I = U \sum_{i=1}^N n_{i\uparrow} n_{i\downarrow}, \quad (5)$$

where U represents the onsite interaction strength.

In this paper we apply the Jordan-Wigner (JW) mapping to transform the fermionic Hubbard Hamiltonian to a qubit representation. The number of terms in the transformed Hamiltonian can be reduced by $2N$ by applying a chemical shift to the interaction term in Eq. (5)

$$H'_I = U \sum_{i=1}^N \left(n_{i\uparrow} - \frac{1}{2} \right) \left(n_{i\downarrow} - \frac{1}{2} \right) = \frac{U}{4} \sum_{i=1}^N Z_{i\uparrow} Z_{i\downarrow}, \quad (6)$$

where $Z_{i\sigma} \equiv 2n_{i\sigma} - 1$. The difference between the original and the shifted on-site interaction term is

$$H'_I - H_I = -\frac{U}{2} \sum_{i=1}^N \left(n_{i\uparrow} + n_{i\downarrow} - \frac{1}{2} \right). \quad (7)$$

In an η -electron subspace, this difference is a constant energy shift of $\Delta E_I = -\frac{U}{2}\eta + \frac{U}{4}N$, which can be trivially corrected [21]. Continuing, we use the modified version (6) of the on-site interaction and refer to it as H_I .

B. The Extended Hubbard Model

We also consider the extended Hubbard model where Coulomb interactions between electrons on neighboring sites are introduced. We define this model as

$$H_{EH} = H_h + H_I + H_V, \quad (8)$$

with $H_C = H_I + H_V$. The Coulomb interaction between neighboring sites is defined as

$$H_V = \frac{V}{2} \sum_{\langle ij \rangle} \sum_{\sigma, \sigma'} n_{i\sigma} n_{j\sigma'}, \quad (9)$$

where V is a parameter for the nearest-neighbor Coulomb interaction. We define the nearest-neighbor summation, $\sum_{\langle ij \rangle}$, to count the interactions between all lattice pairs twice, which is why we multiply by $\frac{1}{2}$. The summation over the spin indices, σ and σ' , ensures that we include interactions between all spin orbitals in lattice pair $\{i, j\}$.

The number of terms in the extended Hubbard model after Jordan-Wigner transformation can be reduced by applying a chemical shift to H_V to obtain

$$\begin{aligned} H'_V &= \frac{V}{2} \sum_{\langle ij \rangle} \sum_{\sigma, \sigma'} \left(n_{i\sigma} - \frac{1}{2} \right) \left(n_{j\sigma'} - \frac{1}{2} \right), \\ &= \frac{V}{8} \sum_{\langle ij \rangle} \sum_{\sigma, \sigma'} Z_{i\sigma} Z_{j\sigma'}. \end{aligned} \quad (10)$$

The difference between the original and the shifted nearest neighbor interaction term is

$$H'_V - H_V = -\frac{V}{4} \sum_{\langle ij \rangle} \sum_{\sigma, \sigma'} \left(n_{i\sigma} + n_{j\sigma'} - \frac{1}{2} \right). \quad (11)$$

Given a k -regular interaction graph with all sites having k nearest neighbors, which is satisfied for periodic lattice models where all sites have k nearest neighbors, then $\sum_{\langle ij \rangle} \sum_{\sigma, \sigma'}$ runs over $4kN$ nearest-neighbor interactions, and the sum over $n_{i\sigma}$ (or $n_{j\sigma'}$) can be rewritten as

$$\sum_{\langle ij \rangle} \sum_{\sigma, \sigma'} n_{i\sigma} = \sum_{i=1}^N \sum_{j: j \sim i} \sum_{\sigma, \sigma'} n_{i\sigma} = 2k \sum_{i=1}^N \sum_{\sigma} n_{i\sigma}, \quad (12)$$

where $\sum_{j: j \sim i}$ is the sum over j neighbor to i and $\sum_{i=1}^N \sum_{\sigma} n_{i\sigma}$ is the total electron number operator.

In an η -electron subspace, Eq. (11) can be written in terms of the total electron number, η , and the total number of lattice sites as

$$\Delta E_V = -\frac{V}{4} \left(4k\eta - \frac{4kN}{4} \right) = \frac{Vk}{4} (N - 4\eta), \quad (13)$$

which is a constant energy shift. From now on we only consider the shifted version (10) of the nearest-neighbor Coulomb interaction term and refer to it as H_V .

III. TILE TROTTERIZATION

In this section, we show how to implement the time evolution operator of generalized Hubbard models using a special variant of second-order Trotterization.

Trotter product formulas approximate the time evolution operator by decomposing the Hamiltonian into m non-commuting terms and then applying the time evolution of these terms sequentially. Hamiltonians of the form $H = \sum_{j=1}^m H_j$ can be approximately evolved for a time t using the second-order Trotter formula

$$\left\| e^{-iHt} - \prod_{j=1}^m e^{-iH_j t/2} \prod_{j=m}^1 e^{-iH_j t/2} \right\| \leq Wt^3, \quad (14)$$

where W is the Trotter error norm given by [61]

$$\begin{aligned} W &= \frac{1}{12} \sum_{b=1}^{m-1} \left\| \sum_{c>b, a>b} [[H_b, H_c], H_a] \right\| \\ &\quad + \frac{1}{24} \sum_{b=1}^{m-1} \left\| \sum_{c>b} [[H_b, H_c], H_b] \right\|, \end{aligned} \quad (15)$$

and where $\|\cdot\|$ is the spectral norm, also known as the operator norm.

The variant of second-order Trotterization described in this paper originates from PLAQ [21], which provides an efficient implementation of the time-evolution operator of square lattice Hubbard models by using a specific structure in both the Hubbard model and the square lattice. PLAQ uses ideas from the SO-FFFT method developed by Kivlichan *et al.* [20], which reduces the Trotter error norm by diagonalizing the hopping Hamiltonian upon each application of $e^{-iH_h t}$. This allows for a simple

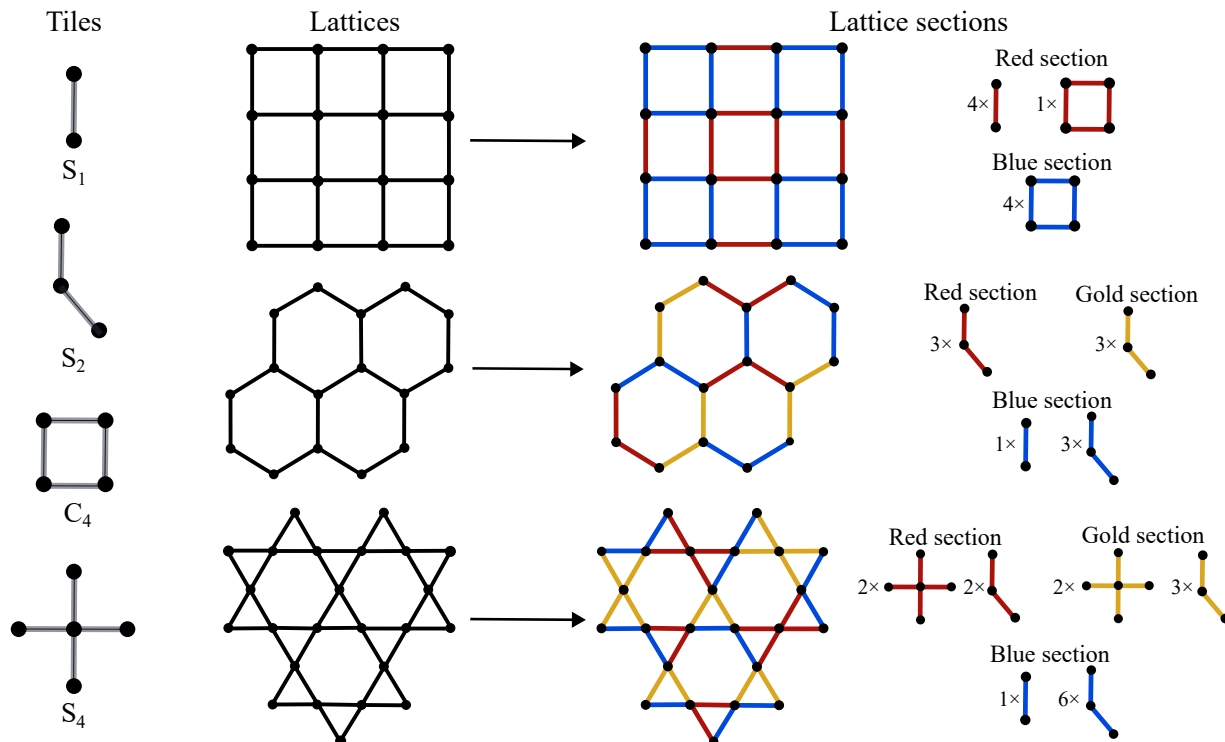


FIG. 1. Illustrations of four tiles, S_1 , S_2 , C_4 and S_4 , and how these tiles can be used to cover three examples of lattice fragments: square, hexagonal and Kagome, in order to create lattice sections. The lattice sections are indicated by different colors: red, blue and gold. On the right, we note how many tiles of the different types are used to cover each lattice section.

Trotter decomposition into two non-commuting groups consisting of hopping terms and Coulomb terms.

A similar Hamiltonian decomposition is used in PLAQ, which also separates the Coulomb and hopping terms. However, instead of simultaneously diagonalizing the hopping terms, they are further decomposed into non-commuting hopping Hamiltonian sections that each can be more easily diagonalized, at the expense of a marginally larger Trotter error norm.

We introduce Tile Trotterization, which allows for quantum simulation of generalized Hubbard models on arbitrary lattices. Although Tile Trotterization can be applied to simulate three-dimensional lattice models, the focus in this paper is on two-dimensional models. The Tile Trotterization scheme is described below, before example applications are discussed in Section IV.

1. Tile Trotterization Scheme

Given a generalized Hubbard model Hamiltonian of the form $H = H_h + H_C$, defined in Eq. (1), the time evolution operator e^{-iHt} can be implemented through Tile Trotterization by separating the hopping Hamiltonian into S non-commuting hopping Hamiltonian sections

$$H_h = \sum_{s=1}^S H_h^s. \quad (16)$$

Each section, H_h^s , consists of N_s tile Hamiltonians in each spin sector that all commute within the same section

$$H_h^s = \sum_{n=1}^{N_s} \sum_{\sigma} H_{\sigma}^{\text{tile},sn}, \quad (17)$$

where the hopping Hamiltonian of the n 'th tile in section s is defined as

$$H_{\sigma}^{\text{tile},sn} = -\tau \sum_{ij} R_{ij}^{\text{tile},sn} a_{i\sigma}^{\dagger} a_{j\sigma}, \quad (18)$$

and $R^{\text{tile},sn}$ is the adjacency matrix of the corresponding tile Hamiltonian.

The tile Hamiltonians, Eq. (18), consist of interactions between neighboring electrons and can be represented as interaction graphs between a set of neighboring lattice points. The decomposition of the hopping Hamiltonian into sections and tiles corresponds to covering the entire lattice by tiles of different colors, where the colors are used as labels for the hopping Hamiltonian sections. These concepts are illustrated in Fig. 1, which shows examples of tiles, lattices, and a possible way to divide these lattices into sections using tiles. The tiles have to cover the entire lattice, and are distributed such that no two tiles within a section touch the same lattice site, ensuring commutativity between all tiles within a section. Note that it is possible to mix different types of tiles to cover a lattice section.

The commutativity of the tile Hamiltonians within a section means that Hamiltonian time evolution of each section can be implemented without Trotter approximation as

$$e^{-iH_h^s t} = \prod_n \prod_\sigma e^{-iH_\sigma^{\text{tile}, sn} t}, \quad (19)$$

such that the cost of implementing $e^{-iH_h^s t}$ can be obtained by counting the number of tiles of different types used to cover the section, given that the cost of implementing $e^{-iH_\sigma^{\text{tile}} t}$ for each tile is known. To obtain the gate cost of $e^{-iH_h^s t}$, the number of each type of tile used in the section is multiplied by two to account for the two spin sectors. As an example, the cost of implementing the red hopping section of the square lattice in Fig. 1 corresponds to 8 applications of $e^{-iH_\sigma^{S1} t}$ and 2 applications of $e^{-iH_\sigma^{C4} t}$.

The cost of implementing $e^{-iH_h^s t}$ can be significantly reduced by choosing tiles with a structure that allows for an efficient implementation of $e^{-iH_\sigma^{\text{tile}} t}$. In particular, $e^{-iH_h^s t}$ can be implemented efficiently and exactly (without further Trotter error) if the tile Hamiltonians are diagonalized upon each application of $e^{-iH_\sigma^{\text{tile}} t}$.

Next, we show that it is possible to choose tiles that can be efficiently diagonalized in order to eliminate the additional Trotter error that would come from a naive implementation of $e^{-iH_\sigma^{\text{tile}} t}$, and we provide a set of tiles that can be used to cover any lattice with nearest-neighbor hopping interactions.

The Hamiltonian of a given tile consists of nearest-neighbor hopping interactions described by an adjacency matrix, R^{tile} . The adjacency matrix of a tile spanning q lattice sites can be represented as a $q \times q$ matrix with

$$R_{ij}^{\text{tile}} = \begin{cases} 1 & \text{if } i \text{ and } j \text{ are neighbors,} \\ 0 & \text{otherwise.} \end{cases} \quad (20)$$

If the entries of the normalized eigenvectors of R^{tile} are integer powers of $\frac{1}{\sqrt{2}}$ then, using the fermionic operators F_{ij} and f_{swap} defined in Appendix A, tile Hamiltonians can be diagonalized without additional synthesis overhead needed to approximate arbitrary rotations. This eigenvector structure occurs in star interaction graphs of type S_{2n} and circle interaction graphs of type C_{2n} , where the subscript denotes the number of edges and n is an integer, including S_1 , S_2 , C_4 (plaquette) and S_4 , as shown in Fig. 1. In Appendix A, we show how these tile Hamiltonians can be diagonalized, and provide gate costings for implementing the time evolution operator of the tile Hamiltonians.

The number of non-zero eigenvalues of R^{tile} is important for determining the cost of Tile Trotterization. If R^{tile} has x non-zero eigenvalues, then implementing $e^{-iH_\sigma^{\text{tile}} t}$ requires x arbitrary rotations, on top of additional T and Clifford gates. The four tiles shown in Fig. 1 all have two non-zero eigenvalues, meaning that

it is more efficient to use the S_2 , C_4 or S_4 tiles to cover lattices over the S_1 tile, as this leads to saving arbitrary rotations. However, the S_1 tile ensures that generalized Hubbard models on arbitrary lattices can be divided into hopping Hamiltonian sections.

The total gate cost of Tile Trotterization also includes an application of $e^{-iH_C t}$. All terms in H_C commute and each term can be implemented without Trotter error using two CNOT gates and one arbitrary Z-axis rotation.

A single Tile Trotterization step of generalized Hubbard model Hamiltonians can be implemented as

$$\left\| e^{-iHt} - e^{-iH_C \frac{t}{2}} \prod_{s=1}^S e^{-iH_h^s \frac{t}{2}} \prod_{s=S}^1 e^{-iH_h^s \frac{t}{2}} e^{-iH_C \frac{t}{2}} \right\| \leq W_{\text{tile}} t^3, \quad (21)$$

where W_{tile} is the Tile Trotterization error norm, which can be bounded using

$$W_{\text{tile}} \leq W_{\text{SO2}} + W_h, \quad (22)$$

as shown in Appendix B. The Trotter error norm W_{SO2} arises from the decomposition into Coulomb and hopping terms

$$\left\| e^{-i(H_h + H_C)t} - e^{-iH_C \frac{t}{2}} e^{-iH_h t} e^{-iH_C \frac{t}{2}} \right\| \leq W_{\text{SO2}} t^3, \quad (23)$$

which is evaluated using the double commutator formula given by Eq. (15). The terminology ‘‘SO2’’ is taken from Ref. [21], and indicates the split-operator decomposition of Coulomb and hopping terms with the ordering employed in Eq. (23). We evaluate W_{SO2} as

$$W_{\text{SO2}} = \frac{1}{12} \|[[H_C, H_h], H_h]\| + \frac{1}{24} \|[[H_C, H_h], H_C]\|. \quad (24)$$

This expression is independent of the hopping sections and the tiles, and captures the total Trotter error norm if the entire hopping Hamiltonian can be diagonalized simultaneously without dividing the lattice into sections.

The additional Trotter error, W_h , depends on the number of sections and the distribution of tiles within each section, and comes from the Trotter decomposition

$$\left\| e^{-iH_h t} - \prod_{s=1}^S e^{-iH_h^s t/2} \prod_{s=S}^1 e^{-iH_h^s t/2} \right\| \leq W_h t^3. \quad (25)$$

This Trotter error norm is generally much smaller than W_{SO2} for physically relevant systems. An expression for W_h can be obtained from Eq. (15) by defining hopping Hamiltonian sections as $H_1 = H_h^1$, $H_2 = H_h^2$, ..., $H_S = H_h^S$, where the subscripts 1, 2 and S denote the order in which the terms are applied in the Trotter decomposition. We explicitly write out Eq. (15) for cases where lattices can be split into three sections in Appendix C, and show how to compute W_h efficiently.

This Trotter error norm structure applies for generalized Hubbard models given by Eq. (1). Therefore, Tile Trotterization can be used to implement the time evolution operator, e^{-iHt} , where H is a generalized Hubbard model, on any lattice using the tiles given in Fig. 1.

IV. APPLICATION OF TILE TROTTERIZATION

Here, we demonstrate how to perform costing of Tile Trotterization in practice. As an example, we consider the more challenging application of the periodic hexagonal lattice extended Hubbard model in the main text. In Appendix E, we give further examples for the Hubbard model on arbitrary hexagonal lattice fragments (models without periodic boundary conditions), and the Hubbard model on a periodic hexagonal lattice. The two periodic models will then be considered in the QPE resource analysis in Section VIC. Note that in Appendix E, we additionally include a discussion on Tile Trotterization for the PPP model.

A. Tile Trotterization of the periodic hexagonal lattice extended Hubbard model: gate counts

We consider the application of Tile Trotterization for simulating the extended Hubbard model on the periodic hexagonal lattice. We use the periodic hexagonal lattice model described in Appendix D which is described by the parameters L_x and L_y and contains $N = 2L_xL_y$ lattice sites.

To apply Tile Trotterization, we cover the periodic hexagonal lattice with S_2 tiles to divide the lattice into three sections: blue (b), red (r) and gold (g), as shown in Fig. 6 in Appendix D. This corresponds to decomposing the hopping Hamiltonian into three sections: $H_h = H_h^b + H_h^r + H_h^g$. The number of S_2 tiles in each section is $N_b = N_r = N_g = N/4$ for all periodic hexagonal lattice models considered in this paper, which have parameters $L_x = L_y = L$.

A single Trotter step of the extended Hubbard model, defined in Eq. (8), on the periodic hexagonal lattice is implemented as

$$e^{-iH_{EH}t} \approx e^{-i(H_I+H_V)\frac{t}{2}} e^{-iH_h^b\frac{t}{2}} e^{-iH_h^r\frac{t}{2}} e^{-iH_h^g\frac{t}{2}} \times e^{-iH_h^r\frac{t}{2}} e^{-iH_h^b\frac{t}{2}} e^{-i(H_I+H_V)\frac{t}{2}}, \quad (26)$$

with $H_{EH} = H_h + H_I + H_V$, and where we choose to implement the sections in the order $H_1 = H_h^b$, $H_2 = H_h^r$ and $H_3 = H_h^g$. Performing r repetitions of this Trotter step leads to

$$\left(e^{-iH_{EH}t} \right)^r \approx e^{-i(H_I+H_V)t} \left(e^{-iH_h^b\frac{t}{2}} e^{-iH_h^r\frac{t}{2}} e^{-iH_h^g\frac{t}{2}} e^{-iH_h^r\frac{t}{2}} e^{-iH_h^b\frac{t}{2}} e^{-i(H_I+H_V)t} \right)^r e^{i(H_I+H_V)\frac{t}{2}}, \quad (27)$$

and therefore a single Trotter step for large r requires two applications of $e^{-iH_h^b t/2}$, two applications of $e^{-iH_h^r t/2}$, one application of $e^{-iH_h^g t}$ and one application of $e^{-i(H_I+H_V)t}$.

Under the Jordan-Wigner transformation, the system is represented by $2N$ qubits and $e^{-i(H_I+H_V)t}$ contains N terms from H_I and $6N$ terms from H_V , which can be implemented with 7 layers of N arbitrary Z -axis rotations,

where the angle of all gates within a given layer are the same, and 14 layers of N CNOT gates.

The cost of implementing the time evolution of the hopping terms is obtained by counting the number of applications of $e^{-iH_{\sigma}^{S_2}t}$ in each section. The time evolution of the hopping Hamiltonian is decomposed into five applications of time evolution of hopping Hamiltonian sections. Each section contains $N/4$ S_2 tiles, so that we need $5 \times \frac{N}{4} \times 2$ applications of $e^{-iH_{\sigma}^{S_2}t}$, accounting for the two spin sectors. The time evolution of each S_2 Hamiltonian can be implemented with 2 arbitrary Z -axis rotations (of the same angle) and 4 T gates, as shown in Appendix A. Therefore, the time evolution of the hopping term can be implemented with 5 layers of N arbitrary rotations of the same angle in each layer. The total non-Clifford gate cost per Trotter step is

$$N_R = 7N + 2 \times \frac{10}{4}N = 12N, \quad (28)$$

$$N_T = 4 \times \frac{10}{4}N = 10N, \quad (29)$$

where N_R is the number of arbitrary rotations and N_T is the number of T gates.

Arbitrary rotations are expensive to perform on fault-tolerant quantum computers using the surface code, most commonly being decomposed into a sequence of T and Clifford gates. Hamming weight phasing (HWP) can be used to reduce the number of arbitrary rotations by trading them for additional ancilla qubits and Toffoli gates. In particular, HWP is applicable when applying a layer of repeated rotation gates of the same angle. In this case, we can introduce ancilla qubits to calculate the Hamming weight of the logical state, and apply a smaller number of rotations to this weight [20, 62]. See also Appendix E2 for more discussion on using HWP for Tile Trotterization.

The time evolution of the extended Hubbard model contains 12 layers of N arbitrary rotations, where the angle of all gates within a given layer are the same. Using HWP, we choose to implement m arbitrary rotations simultaneously using $m - 1$ ancilla qubits, with the requirement that N is an integer multiple of m , leading to a worst case total gate cost of [21]

$$N_R = \frac{12N}{m} [\log_2(m) + 1], \quad (30)$$

$$N_T = 10N + 4 \times \frac{12N}{m} (m - 1), \quad (31)$$

where each Toffoli gate has been converted into 4 T gates. The total number of qubits required for this Tile Trotterization implementation with HWP is $2N + (m - 1)$.

B. Tile Trotterization of the periodic hexagonal lattice extended Hubbard model: error bounds

The error norm can be obtained from Eq. (22), and W_{SO_2} can be evaluated using Eq. (24). We prove in

Lemma F.1 in Appendix F that $\|[[H_C, H_h], H_C]\|$, with $H_C = H_I + H_V$, can be evaluated as

$$\begin{aligned} \|[[H_C, H_h], H_C]\| &\leq (U^2 + kV^2)\|H_h\| \\ &+ \left((4k-2)\tau UV + (k-1)(4k-1)\tau V^2\right)kN, \end{aligned} \quad (32)$$

for lattices where each lattice site has k nearest neighbors. Using that $k = 3$ for the periodic hexagonal lattice, we obtain

$$\begin{aligned} \|[[H_C, H_h], H_C]\| &\leq (\tau U^2 + 3\tau V^2)\|R\|_1 \\ &+ (30\tau UV + 66\tau V^2)N, \end{aligned} \quad (33)$$

where R is the adjacency matrix of the periodic hexagonal lattice and $\|\cdot\|_1$ is the Schatten one-norm.

The second commutator is bounded using the triangle inequality

$$\|[[H_C, H_h], H_h]\| \leq \|[[H_I, H_h], H_h]\| + \|[[H_V, H_h], H_h]\|. \quad (34)$$

We use Lemma 2 in Appendix C of Ref. [21] to bound $\|[[H_I, H_h], H_h]\|$ as

$$\|[[H_I, H_h], H_h]\| \leq 14U\tau^2 N. \quad (35)$$

For more details on how to obtain this bound, we refer to the evaluation of commutator bounds of Hubbard model systems in Appendix E.

We show in Lemma F.3 of Appendix F that for lattices where each lattice site has k neighbors, $\|[[H_V, H_h], H_h]\|$ can be evaluated as

$$\begin{aligned} \|[[H_V, H_h], H_h]\| &\leq V k N \left(\|[[H_{k-1, \sigma}, H_h]\| + 4\|H_{k-1, \sigma}\|^2 \right. \\ &\quad \left. + \|[[H_{k, \sigma}, H_h]\| + 2\|H_{k, \sigma}\|^2 \right), \end{aligned} \quad (36)$$

where $H_{k-1, \sigma}$ and $H_{k, \sigma}$ are local hopping operators defined in Eq. (F54). This expression can be easily evaluated by noting that $H_{k-1, \sigma}$, $H_{k, \sigma}$ and H_h are free fermionic operators, as discussed in Appendix F.1. In Corollary F.4 in Appendix F, we show that the bound in Eq. (36) can be evaluated for the periodic hexagonal lattice as

$$\|[[H_V, H_h], H_h]\| \leq 3V\tau^2 N(16 + 2\sqrt{3}). \quad (37)$$

We obtain W_h as shown in Appendix C, where Eq. (C6) gives a formula for efficiently evaluating the hopping Hamiltonian error norm for the hopping Hamiltonian decomposition used here. In the numerical examples for the extended Hubbard model given in this paper with $U = 4$, $V = 2$ and $\tau = 1$, we find that W_h constitutes around 2.2% of the total Trotter error norm W_{tile} .

Overall, we find that the Tile Trotterization error norm, W_{tile} , for the periodic hexagonal lattice extended Hubbard model scales as $\mathcal{O}(N)$, which is the same scaling as for the Hubbard model systems discussed in Appendices E.1 and E.2.

V. QUBITIZATION FOR THE HEXAGONAL HUBBARD MODEL

The discussion so far has focused on quantum simulation using Tile Trotterization. In order to assess this approach, we will next consider qubitization, which is a state-of-the-art approach for performing quantum simulation, therefore providing an important comparison point [38–40]. In Appendix H, we provide quantum circuits for the qubitized quantum walk operator for the periodic hexagonal Hubbard model, and include detailed resource estimates. Our construction of the qubitization circuit follows that developed in Ref. [40], but we introduce improvements that further reduce resource estimates, and perform costing of all circuit elements in detail. For brevity, in this section we briefly summarize the key costs to perform qubitized QPE using these circuits, which will be used to perform resource estimation of QPE in Section VI.

The quantum walk operator used in qubitization consists of SELECT, PREPARE and reflection operations. For the Hubbard model, the asymptotically dominant cost of performing qubitized QPE comes from implementing SELECT (controlled on an ancilla). For an $L_x \times L_y$ hexagonal lattice we obtain a T gate cost of $C_S = 40L_x L_y - 4$, or, expressed in terms of the number of lattice points, N ,

$$C_S = 20N - 4. \quad (38)$$

Note that the $\mathcal{O}(N)$ term is identical to that obtained in Ref. [40] for the square lattice, but our circuit removes an additional $\mathcal{O}(\log(N))$ contribution.

The cost of PREPARE is more involved, and we summarize the cost of each circuit element in Table III in Appendix H. Summing the contribution from each of these elements, and taking the case where $L_x = L_y = L$, the total T gate cost of PREPARE is

$$C_P = 46\lceil \log_2 L \rceil + 4\Theta + 4\Gamma - 24\eta_L - 16, \quad (39)$$

where η_L is the largest power of 2 that is a factor of L , Θ is the number of T gates per rotation in the UNIFORM state preparation gadgets, and Γ is the number of T gates per each other rotation in PREPARE. Therefore, the cost of PREPARE is only logarithmic in the lattice dimension, L . For our resource estimates, we choose $\Theta = 10$ and $\Gamma = 40$.

The controlled reflection operator adds an additional T gate cost of

$$C_R = 32\lceil \log_2 L \rceil + 77, \quad (40)$$

using the scheme of Ref. [63] to perform the reflection with a single ancilla qubit.

The controlled walk operator also requires additional flag and ancilla qubits. Once again taking the case of $L_x = L_y = L$, the total number of qubits to implement the circuits in Appendix H is

$$N_{\text{qubits}} = 2N + 6\lceil \log_2 L \rceil + 15. \quad (41)$$

VI. QUANTUM PHASE ESTIMATION

In this section, we provide resource estimates for QPE based on Tile Trotterization and qubitization. We begin by describing the QPE schemes used for each method.

A. Trotterized QPE

We follow the quantum phase estimation costing procedure for Trotterization methods described by Kivlichan *et al.* in Ref. [20]. This phase estimation scheme relies on adaptive phase estimation techniques [64, 65] which use a single control qubit. We define the maximum allowed error in the energy estimate as ϵ , and following Ref. [21], assign $x\epsilon$ of the total error to rotation synthesis error and $(1-x)\epsilon$ to Trotter error and phase estimation error. This allows us to determine the total number of Trotter steps required for the phase estimation procedure as [20, 21]

$$N_{\text{PE}} = 6.203 \frac{\sqrt{W}}{(1-x)^{3/2} \epsilon^{3/2}}, \quad (42)$$

where W is the Trotter error norm.

The T gate cost per Trotter step from synthesis of rotation gates, N_{RT} , using repeat-until-success synthesis [66], can be evaluated as [21]

$$N_{RT} = N_R \left(1.15 \log_2 \left(\frac{N_R \sqrt{3W}}{x \sqrt{1-x} \epsilon^{3/2}} \right) + 9.2 \right), \quad (43)$$

where N_R is the number of arbitrary rotations per Trotter step. The total T gate cost for performing Trotterized QPE is given by

$$N_{T, \text{Trotter}} = N_{\text{PE}}(N_{RT} + N_T), \quad (44)$$

where N_T is the number of T gates per Trotter step that do not come from the synthesis of arbitrary rotations.

To assess the T gate complexity, note that the number of Trotter steps scales as $N_{\text{PE}} = \mathcal{O}(N^{1/2} \epsilon^{-3/2})$ for the Hubbard model and extended Hubbard model, and the T gate cost per step *aside from rotation synthesis* is $N_T = \mathcal{O}(N)$. If HWP is applied, then $N_R = \mathcal{O}(\log(N))$ (from Eq. (30)) in which case N_{RT} does not contribute asymptotically, resulting in a T gate complexity of

$$\mathcal{O}(N^{3/2} \epsilon^{-3/2}). \quad (45)$$

If HWP is not applied then $N_R = \mathcal{O}(N)$ (from Eq. (28)), and the overall T complexity picks up a logarithmic factor

$$\mathcal{O}(N^{3/2} \epsilon^{-3/2} \log(N \epsilon^{-1})). \quad (46)$$

In practice, the precision of rotation synthesis can be improved with low additional cost, and the number of T gates per arbitrary rotation is often set as a constant, meaning the logarithmic factor can be disregarded. The scaling with and without HWP reported here applies for

both the extended Hubbard model (Sec. IV) and the Hubbard model systems (E1 and E2). The Hubbard model systems however have smaller prefactors coming from lower W_{SO2} and fewer arbitrary rotation layers.

The phase estimation procedure used for Tile Trotterization requires two qubits in addition to the $2N$ system qubits: one for adaptive phase estimation and one for repeat-until-success synthesis [20, 21]. Through numerical tests of the overall T gate cost, we find that optimal values of x are approximately $x = 0.03$ without applying HWP and $x = 0.01$ with HWP.

B. Qubitized QPE

For qubitized QPE, we follow the phase estimation scheme described in Ref. [6], which uses $N_{\mathcal{W}}$ repetitions of the qubitized quantum walk operator, \mathcal{W} , which consists of the operators controlled SELECT (S), PREPARE (P), PREPARE † (P †) and controlled reflection (R). The number of repetitions of the qubitized quantum walk operator is given by

$$N_{\mathcal{W}} = \left\lceil \frac{\pi \lambda}{2\epsilon} \right\rceil, \quad (47)$$

where λ is the L1 norm and ϵ is the allowed error in phase estimation. For the periodic hexagonal lattice Hubbard model, the L1 norm is

$$\lambda = \left(3\tau + \frac{U}{4} \right) N. \quad (48)$$

The total qubitized QPE T gate cost is

$$N_{T, N_{\mathcal{W}}} = \left\lceil \frac{\pi \lambda}{2\epsilon} \right\rceil (C_S + C_P + C_{P^\dagger} + C_R), \quad (49)$$

where C_Q represents the T gate cost of operation Q . Note that our implementation has the same cost for P and P † . The T gate complexity of qubitized QPE on the periodic hexagonal lattice Hubbard model scales as

$$\mathcal{O}(N^2 \epsilon^{-1}). \quad (50)$$

Note that this phase estimation scheme uses $\alpha_{PE} = 2 \lceil \log_2(N_{\mathcal{W}} + 1) \rceil - 1$ ancilla qubits for the control register [6, 67], in addition to the qubits quoted in Eq. (41). Therefore, the number of qubits depend on the Hubbard model parameters, U and τ , as well as ϵ . The unary iterator over the walk operator also requires $(4N_{\mathcal{W}} - 4)$ T gates to implement, in addition to the per-walk operator T gate counts given in Eq. (49).

C. QPE resource estimates

In our QPE resource estimates, we disregard the cost of state preparation, although this is an important and non-trivial problem [68]. Efforts have been made to efficiently prepare correlated fermionic states of Hubbard

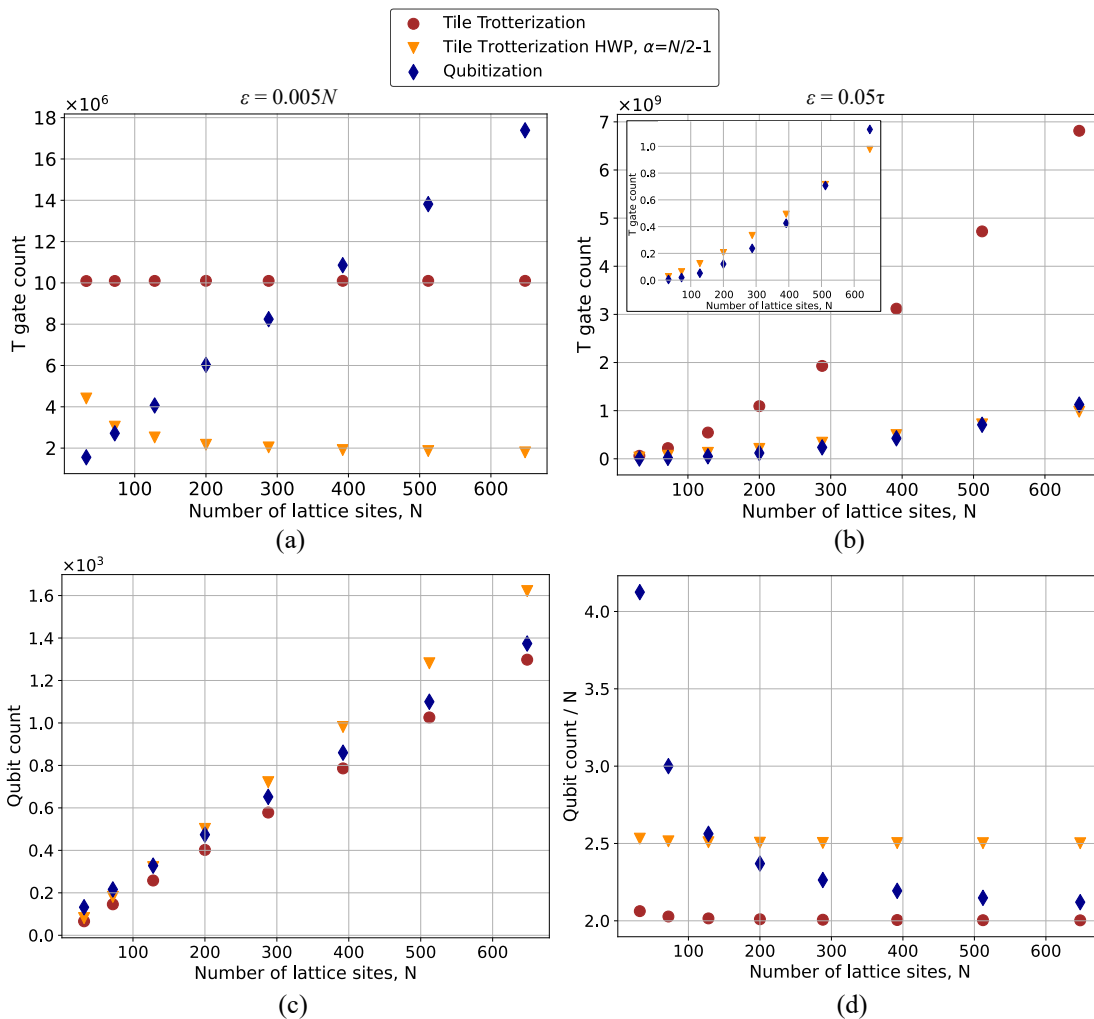


FIG. 2. Resource estimates for QPE performed on a periodic hexagonal lattice Hubbard model with $L_x = L_y = L$, using Tile Trotterization (see Appendix E 2), Tile Trotterization HWP (Hamming weight phasing; with $\alpha = N/2 - 1$ ancilla qubits, see Appendix E 2), and qubitization (see Sec. V). (a) Total T gate count as a function of the number of lattice sites, N , with $\epsilon = 0.005N$. (b) Total T gate count as a function of the number of lattice sites, N , with $\epsilon = 0.05\tau$. The inset shows the total T gate count for Tile Trotterization HWP and qubitization. Note that the total T gate counts of Tile Trotterization based QPE are upper bounds. (c) The total number of qubits used for each method. (d) The total number of qubits used for each method, divided by N .

models on quantum computers [50, 69]. The state preparation problem, and its cost for Hubbard models, is further discussed in Yoshioka *et al.* [14]. We will continue by assuming that an initial state can be prepared with a sufficient overlap with the target state.

In Table II of Appendix G we provide Tile Trotterization error norms, qubit counts, arbitrary rotation costs and T costs per Trotter step to perform the simulations considered in this section. The qubitization cost is obtained from Eq. (49), with the cost of each quantum walk operator element given by Eqs. (38)–(40).

We begin our QPE resource analysis by comparing the performance of Tile Trotterization (Appendix E 2) with our qubitization based approach (Sec. V) for simulating the periodic hexagonal lattice Hubbard model. This is done to highlight the difference in scaling and perfor-

mance of the two approaches for different system sizes N , and for different maximum errors ϵ . The comparison between Tile Trotterization and qubitization is shown in Fig. 2, where the resource requirements of Tile Trotterization, Tile Trotterization with HWP using $\alpha = N/2 - 1$ ancillas, and qubitization for performing QPE on the periodic hexagonal lattice Hubbard model with parameters $L_x = L_y = L$, $U = 4$ and $\tau = 1$ are plotted as a function of the number of lattice sites, N .

Fig. 2(a) presents the total T gate count as a function of the number of lattice sites, N , and taking the case where ϵ scales with the system size as $\epsilon = 0.005N$. The T gate cost of qubitized QPE is lower than for Trotterized QPE for small systems but grows linearly with N using this choice of ϵ , eventually becoming more expensive than both Trotterization methods. On the other hand, the

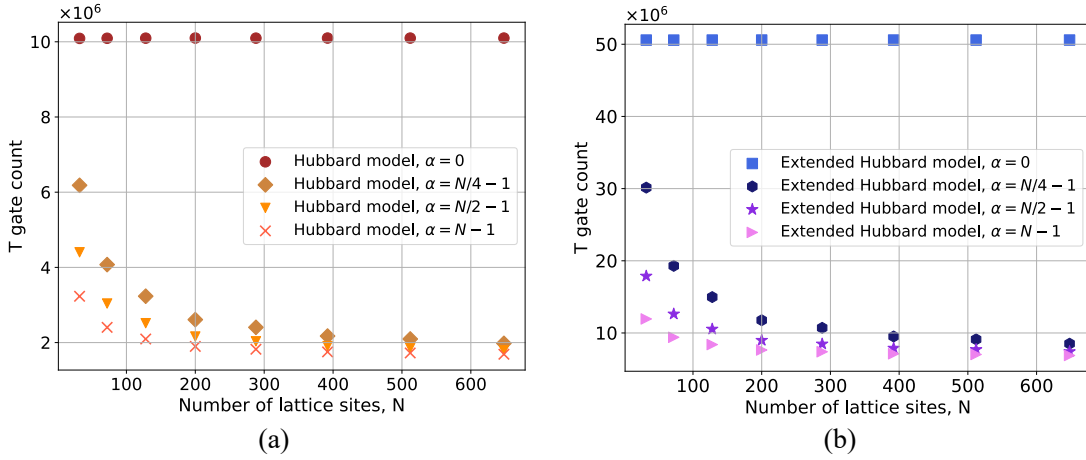


FIG. 3. Upper bounds on the total T gate count for performing QPE with Tile Trotterization on periodic hexagonal lattice Hubbard models with $L_x = L_y = L$ and $\epsilon = 0.005N$, as a function of the number of lattice sites, N . We compare four different simulation approaches with $\alpha = 0$, $\alpha = N/4 - 1$, $\alpha = N/2 - 1$ and $\alpha = N - 1$ ancilla qubits for HWP for the two models: (a) Hubbard model (see Appendix E 2) and (b) Extended Hubbard model (see Sec. IV).

cost of Tile Trotterization remains constant here for ϵ scaling with N . The Tile Trotterization HWP simulation also asymptotically approaches a constant value around 1.8×10^6 total T gates with increasing N . The total T gate cost of Tile Trotterization HWP is dominated by $\log(N)$ -terms from the number of arbitrary rotations per Trotter step, N_{RT} , at small N , and therefore the total T gate cost decreases with increasing N , as the logarithmic term is suppressed by the linearly growing ϵ . Eventually, the linearly growing N_T demoniates the total T gate cost per Trotter step, such that the total T gate count approaches a constant value.

Fig. 2(b) shows the total T gate count as a function of N , with a fixed allowed error of $\epsilon = 0.05\tau$. The inset in the top-left corner shows the T gate cost for Tile Trotterization HWP and qubitization only, to more clearly display their different scaling, $\mathcal{O}(N^{3/2})$ for Tile Trotterization HWP and $\mathcal{O}(N^2)$ for qubitization. We once again see that the qubitization approach performs better than Tile Trotterization HWP for the smaller systems considered, because of the relatively low ϵ , but Tile Trotterization HWP eventually obtains lower T gate cost due to its better system size scaling. For maximum errors of $\epsilon \geq 0.26\tau$, Tile Trotterization HWP achieves lower T gate cost than qubitization for the models considered with $N \geq 128$.

These results only demonstrate the total T gate cost of periodic Hubbard model simulations. We note that simulating hexagonal lattice fragments (non-periodic models or nanographene) with Tile Trotterization (Appendix E 1) will have slightly lower cost than for periodic Hubbard models with the same number of lattice sites. This is because the average number of bonds from each site will be less than 3 since fragments contain edge sites (see Fig. 8). This means that the fragment Hubbard models have fewer hopping terms resulting in fewer tiles and lower gate cost per section, lower W_{SO2} (Eqs. (E5)

and (E6)) and lower W_h .

Fig. 2(c) presents the number of qubits used for the three simulation methods, and Fig. 2(d) shows the qubit count divided by N to make it easier to see the differences in qubit counts. We have chosen $U = 4$, $\tau = 1$ and $\epsilon = 0.05\tau$ for the qubitization-based qubit count; the Trotter qubit counts are independent of these parameters. These figures show that the qubit counts for the three approaches are comparable and scale similarly. However, for small lattice sizes, the qubitization-based approach requires significantly more ancilla qubits relative to the $2N$ system qubits.

Next, we compare the T gate costs between different Hubbard model and extended Hubbard model simulation methods. The qubit counts using α ancilla qubits is the same for the Hubbard model and the extended Hubbard model simulations. Fig. 3 presents a comparison between Trotterized QPE resource estimates for the standard Hubbard model and the extended Hubbard model, and also the effect of varying the number of ancilla qubits, α , used for the HWP procedure. In these plots we take a target accuracy of $\epsilon = 0.005N$.

For the Hubbard model costings shown in Fig. 3(a), we provide four examples using $\alpha = 0$, $\alpha = N/4 - 1$, $\alpha = N/2 - 1$ and $\alpha = N - 1$ ancilla qubits for HWP, where the $\alpha = 0$ and $\alpha = N/2 - 1$ results correspond to those also shown in Fig. 2(a). The difference in T gate cost for different α is greater for small N because the cost in this regime is dominated by $\log(N)$ terms with different constant factors, as shown in Eq. (E13), that will be suppressed by ϵ growing linearly in N . The T gate cost of the Tile Trotterization HWP simulations asymptotically approaches the same constant value dominated by N_T , as given by Eq. (E16).

The extended Hubbard model simulation costings shown in Fig. 3(b) behave similarly to the Hubbard model simulations, but requires around four to five times

more T gates across the range of system sizes considered here. The additional cost comes from the larger Trotter error norm for the extended Hubbard model combined with the higher gate count per Trotter step. The T gate cost for simulating the extended Hubbard model using Tile Trotterization with HWP for $\epsilon = 0.005N$ approaches a value around 7×10^6 , for large N .

VII. DISCUSSION AND OUTLOOK

This paper presents a Trotterization method that can be used to implement the time evolution operator for generalized Hubbard models on arbitrary lattices. Tile Trotterization allows for constructing efficient Trotter decompositions and provides a straightforward method to obtain per-Trotter-step gate counts, and a procedure to calculate Trotter error bounds. Tile Trotterization can also be combined with Hamming weight phasing in order to significantly reduce the number of arbitrary rotation gates required per Trotter step.

We demonstrated applications of Tile Trotterization for energy estimation by QPE for both the Hubbard model and the extended Hubbard model with nearest-neighbor Coulomb interactions, showing that the method achieves a T gate complexity $\mathcal{O}(N^{3/2}\epsilon^{-3/2})$, where N is the number of lattice sites and ϵ is the maximum allowed error in the energy. In order to perform resource estimates for the extended Hubbard model, we derived new commutator bounds, given by Eqs. (32) and (36). The same asymptotic scaling can be achieved for other local Hubbard models, for example on the square lattice or the Kagome lattice, and for non-periodic lattice models, given that the lattice can be divided into sections as illustrated in Fig. 1. Tile Trotterization also provides a framework for simulating more complicated and non-local models such as the PPP model, which more closely resemble the full electronic structure Hamiltonian.

We also constructed and optimized the qubitized quantum walk operator for the hexagonal lattice Hubbard model and provided detailed Toffoli gate, T gate and qubit counts. These were used to perform resource estimation for qubitized quantum phase estimation, demonstrating a T gate complexity of $\mathcal{O}(N^2\epsilon^{-1})$. The Trotterization-based QPE approach studied in this paper has better scaling with respect to system size, which results in lower T gate counts for simulations of large systems, especially when ϵ is allowed to scale extensively with N .

The results presented here demonstrate that a range of classically non-trivial model Hamiltonians instances can be simulated with 10^6 – 10^7 non-Clifford gates. This is several orders of magnitude less than found in many resource estimation studies of *ab initio* chemical systems, suggesting that such model Hamiltonians are promising candidate applications for early fault-tolerant quantum computers. Going forward, it will be important to consider more detailed costing of this problem for early fault-

tolerant architectures. Current resource estimates focus on counting non-Clifford gates, which have historically been expected to be most expensive to perform under traditional QEC schemes. However, recent proposals have questioned this understanding [70]. Previous resource estimates have also focused on particular architectures where the cost of Clifford gates can be ignored [71], which may not be appropriate for early FT devices. Therefore, an interesting and important task is to consider a more detailed compilation to an early FT architecture. Here, relevant questions include: how routing can be efficiently performed under lattice surgery; how gates may be best parallelized; and efficient schemes for performing rotation gates with lower costs. An attempt at this was recently performed in Ref. [16], using the STAR architecture [72] and an alternative Trotter scheme than the one presented here.

Performing such a compilation to an early fault-tolerant architecture will introduce a number of considerations beyond those discussed in this paper. These include, for example, the cost of Clifford gates under lattice surgery and the parallelizability of a given logical circuit. We expect that the Tile Trotterization scheme here is a particularly promising candidate for such early FT applications. In addition to the low gate count, circuits are relatively simple, consisting of just a small number of rotation gate layers per Trotter step (in addition to fermionic swap layers). Such considerations will also affect the efficiency of various schemes; for example, the Hamming weight phasing method considered in this work reduces the number of rotation gates, but at the cost of additional qubits, two-qubit gates and significantly reduced parallelizability. Indeed, applying HWP to implement a single layer of n rotation gates requires $n - 1$ Toffoli gates in adder circuits, which cannot be readily parallelized; given these costs, it remains to be seen if applying HWP would give any advantage when implemented in a practical FT architecture. Separately, we also note that the Tile Trotterization scheme could be performed in combination with early fault-tolerant algorithms such as statistical phase estimation to significantly reduce circuit depths compared to those presented here [32, 73]. The scheme presented in this paper also allows for significantly more complicated model Hamiltonians, such as the PPP model, which provide a link to *ab initio* quantum chemistry. Given all of these benefits, and the significant challenge of performing dynamics of model Hamiltonians in strongly correlated regimes by conventional methods, we believe that this is a promising area for practical quantum algorithms going forward.

ACKNOWLEDGMENTS

This work is supported by the Novo Nordisk Foundation, Grant number NNF22SA0081175, NNF Quantum Computing Programme. We thank Matthew S. Teynor and Earl T. Campbell for feedback on the manuscript.

- [1] R. P. Feynman, *International Journal of Theoretical Physics* **21**, 467 (1982).
- [2] S. Lloyd, *Science* **273**, 1073 (1996).
- [3] I. Kassal, S. P. Jordan, P. J. Love, M. Mohseni, and A. Aspuru-Guzik, *Proceedings of the National Academy of Sciences of the United States of America* **105**, 18681 (2008).
- [4] M. Reiher, N. Wiebe, K. M. Svore, D. Wecker, and M. Troyer, *Proceedings of the National Academy of Sciences of the United States of America* **114**, 7555 (2017).
- [5] J. J. Goings, A. White, J. Lee, C. S. Tautermann, M. Degroote, C. Gidney, T. Shiozaki, R. Babbush, and N. C. Rubin, *Proceedings of the National Academy of Sciences* **119**, e2203533119 (2022), <https://www.pnas.org/doi/pdf/10.1073/pnas.2203533119>.
- [6] J. Lee, D. W. Berry, C. Gidney, W. J. Huggins, J. R. McClean, N. Wiebe, and R. Babbush, *PRX Quantum* **2**, 030305 (2021).
- [7] D. W. Berry, C. Gidney, M. Motta, J. R. McClean, and R. Babbush, *Quantum* **3**, 208 (2019).
- [8] H. H. S. Chan, R. Meister, T. Jones, D. P. Tew, and S. C. Benjamin, *Science Advances* **9**, eabo7484 (2023).
- [9] I. D. Kivlichan, N. Wiebe, R. Babbush, and A. Aspuru-Guzik, *Journal of Physics A: Mathematical and Theoretical* **50** (2017), 10.1088/1751-8121/aa77b8.
- [10] A. V. Ivanov, C. Sünderhauf, N. Holzmann, T. Ellaby, R. N. Kerber, G. Jones, and J. Camps, *Phys. Rev. Res.* **5**, 013200 (2023).
- [11] R. Babbush, N. Wiebe, J. McClean, J. McClain, H. Neven, and G. K.-L. Chan, *Phys. Rev. X* **8**, 011044 (2018).
- [12] N. C. Rubin, D. W. Berry, F. D. Malone, A. F. White, T. Khattar, A. E. DePrince, S. Siculo, M. Kühn, M. Kaicher, J. Lee, and R. Babbush, *PRX Quantum* **4**, 040303 (2023).
- [13] J. Hubbard, *Proceedings of the Royal Society of London. Series A, Mathematical and Physical Sciences* **276**, 238 (1963).
- [14] N. Yoshioka, T. Okubo, Y. Suzuki, Y. Koizumi, and W. Mizukami, *npj Quantum Information* **10**, 45 (2024).
- [15] R. Toshio, Y. Akahoshi, J. Fujisaki, H. Oshima, S. Sato, and K. Fujii, (2024), [arXiv:2408.14848 \[quant-ph\]](https://arxiv.org/abs/2408.14848).
- [16] Y. Akahoshi, R. Toshio, J. Fujisaki, H. Oshima, S. Sato, and K. Fujii, (2024), [arXiv:2408.14929 \[quant-ph\]](https://arxiv.org/abs/2408.14929).
- [17] X. Dong, L. D. Re, A. Toschi, and E. Gull, *Proceedings of the National Academy of Sciences* **119**, e2205048119 (2022).
- [18] J. Kaczmarczyk, J. Spałek, T. Schickling, and J. Bünenmann, *Phys. Rev. B* **88**, 115127 (2013).
- [19] P. A. Lee, N. Nagaosa, and X.-G. Wen, *Rev. Mod. Phys.* **78**, 17 (2006).
- [20] I. D. Kivlichan, C. Gidney, D. W. Berry, N. Wiebe, J. McClean, W. Sun, Z. Jiang, N. Rubin, A. Fowler, A. Aspuru-Guzik, H. Neven, and R. Babbush, *Quantum* **4**, 296 (2020).
- [21] E. T. Campbell, *Quantum Science and Technology* **7**, 015007 (2021).
- [22] H. F. Trotter, *Proceedings of the American Mathematical Society* **10**, 545 (1959).
- [23] M. Suzuki, *J. Math. Phys.* **32**, 400 (1991).
- [24] J. B. James D. Whitfield and A. Aspuru-Guzik, *Molecular Physics* **109**, 735 (2011).
- [25] A. Y. Kitaev, (1995), [arXiv:quant-ph/9511026 \[quant-ph\]](https://arxiv.org/abs/quant-ph/9511026).
- [26] D. S. Abrams and S. Lloyd, *Phys. Rev. Lett.* **83**, 5162 (1999).
- [27] R. Cleve, A. Ekert, C. Macchiavello, and M. Mosca, *Proceedings of the Royal Society of London. Series A: Mathematical, Physical and Engineering Sciences* **454**, 339 (1998).
- [28] A. Aspuru-Guzik, A. D. Dutoi, P. J. Love, and M. Head-Gordon, *Science* **309**, 1704 (2005).
- [29] R. D. Somma, *New Journal of Physics* **21**, 123025 (2019).
- [30] L. Lin and Y. Tong, *PRX Quantum* **3**, 010318 (2022).
- [31] K. Wan, M. Berta, and E. T. Campbell, *Phys. Rev. Lett.* **129**, 030503 (2022).
- [32] G. Wang, D. S. França, R. Zhang, S. Zhu, and P. D. Johnson, *Quantum* **7**, 1167 (2023).
- [33] N. S. Blunt, L. Caune, R. Izsák, E. T. Campbell, and N. Holzmann, *PRX Quantum* **4**, 040341 (2023).
- [34] Z. Ding, C.-F. Chen, and L. Lin, *Phys. Rev. Res.* **6**, 033147 (2024).
- [35] H.-E. Li, Y. Zhan, and L. Lin, (2024), [arXiv:2411.01470 \[quant-ph\]](https://arxiv.org/abs/2411.01470).
- [36] C.-F. Chen, M. J. Kastoryano, F. G. S. L. Brandão, and A. Gilyén, (2023), [arXiv:2303.18224 \[quant-ph\]](https://arxiv.org/abs/2303.18224).
- [37] G. H. Low and I. L. Chuang, *Quantum* **3**, 163 (2019).
- [38] D. W. Berry, M. Kieferová, A. Scherer, Y. R. Sanders, G. H. Low, N. Wiebe, C. Gidney, and R. Babbush, *npj Quantum Information* **4**, 22 (2018).
- [39] D. Poulin, A. Kitaev, D. S. Steiger, M. B. Hastings, and M. Troyer, *Phys. Rev. Lett.* **121**, 010501 (2018).
- [40] R. Babbush, C. Gidney, D. W. Berry, N. Wiebe, J. McClean, A. Paler, A. Fowler, and H. Neven, *Phys. Rev. X* **8**, 041015 (2018).
- [41] A. Kan and B. Symons, “Resource-optimized fault-tolerant simulation of the fermi-hubbard model and high-temperature superconductor models,” (2024), [arXiv:2411.02160 \[quant-ph\]](https://arxiv.org/abs/2411.02160).
- [42] Y. Yu, S. Li, S. Isakov, and E. Gull, *Physical Review B* **107**, 075106 (2023).
- [43] C. Wen, X. Zhu, Z. Xiao, N. Hao, R. Mondaini, H. Guo, and S. Feng, *Phys. Rev. B* **105**, 075118 (2022).
- [44] F. Ferrari, F. Becca, and R. Valentí, *Phys. Rev. B* **106**, L081107 (2022).
- [45] J. B. Profe, L. Klebl, F. Grandi, H. Hohmann, M. Dürrnagel, T. Schwemmer, R. Thomale, and D. M. Kennes, *Phys. Rev. Res.* **6**, 043078 (2024).
- [46] J. Paki, H. Terletska, S. Isakov, and E. Gull, *Phys. Rev. B* **99**, 245146 (2019).
- [47] S.-Z. Zhou, K. Cheng, and Z.-B. Huang, *Results in Physics* **61**, 107748 (2024).
- [48] T. Schwemmer, H. Hohmann, M. Dürrnagel, J. Potten, J. Beyer, S. Rachel, Y.-M. Wu, S. Raghu, T. Müller, W. Hanke, and R. Thomale, *Phys. Rev. B* **110**, 024501 (2024).
- [49] M. Schüler, M. Rösner, T. O. Wehling, A. I. Lichtenstein, and M. I. Katsnelson, *Phys. Rev. Lett.* **111**, 036601 (2013).
- [50] P.-L. Dallaire-Demers, J. Romero, L. Veis, S. Sim, and A. Aspuru-Guzik, *Quantum Science and Technology* **4**, 045005 (2019).

- [51] T. G. Schmalz, L. Serrano-Andrés, V. Sauri, M. Merchán, and J. M. Oliva, *The Journal of Chemical Physics* **135**, 194103 (2011).
- [52] Y. Yoshida, N. Takemori, and W. Mizukami, *The Journal of Chemical Physics* **161**, 084303 (2024).
- [53] A. L. Szabó and B. Roy, *Phys. Rev. B* **103**, 205135 (2021).
- [54] J. A. Pople, *Transactions of the Faraday Society* **49**, 1375 (1953).
- [55] R. Pariser and R. G. Parr, *The Journal of Chemical Physics* **21**, 466 (1953).
- [56] T. G. Schmalz, *Croatica Chemica Acta* **86**, 419 (2013).
- [57] S. Mishra, D. Beyer, K. Eimre, S. Kezilebieke, R. Berger, O. Gröning, C. A. Pignedoli, K. Müllen, P. Liljeroth, P. Ruffieux, X. Feng, and R. Fasel, *Nature Nanotechnology* **15**, 22 (2020).
- [58] S. Song, A. Pinar Solé, A. Matěj, G. Li, O. Stetsovych, D. Soler, H. Yang, M. Telychko, J. Li, M. Kumar, Q. Chen, S. Edalatmanesh, J. Brabec, L. Veis, J. Wu, P. Jelinek, and J. Lu, *Nature Chemistry* **2024** 16:6 **16**, 938 (2024).
- [59] E. V. Boström, A. Mikkelsen, C. Verdozzi, E. Perfetto, and G. Stefanucci, *Nano Letters* **18**, 785 (2018).
- [60] J. Aftab, D. An, and K. Trivisa, (2024), [arXiv:2403.08922 \[quant-ph\]](#).
- [61] A. M. Childs, Y. Su, M. C. Tran, N. Wiebe, and S. Zhu, *Phys. Rev. X* **11**, 011020 (2021).
- [62] C. Gidney, *Quantum* **2**, 74 (2018).
- [63] T. Khattar and C. Gidney, (2024), [arXiv:2407.17966 \[quant-ph\]](#).
- [64] D. W. Berry, B. L. Higgins, S. D. Bartlett, M. W. Mitchell, G. J. Pryde, and H. M. Wiseman, *Phys. Rev. A* **80**, 052114 (2009).
- [65] B. L. Higgins, D. W. Berry, S. D. Bartlett, H. M. Wiseman, and G. J. Pryde, *Nature* **2007** 450:7168 **450**, 393 (2007).
- [66] A. Bocharov, M. Roetteler, and K. M. Svore, *Phys. Rev. Lett.* **114**, 080502 (2015).
- [67] T. N. Georges, M. Bothe, C. Sünderhauf, B. K. Berntson, R. Izsák, and A. V. Ivanov, (2024), [arXiv:2408.03145 \[quant-ph\]](#).
- [68] S. Lee, J. Lee, H. Zhai, Y. Tong, A. M. Dalzell, A. Kumar, P. Helms, J. Gray, Z. H. Cui, W. Liu, M. Kastyano, R. Babbush, J. Preskill, D. R. Reichman, E. T. Campbell, E. F. Valeev, L. Lin, and G. K. L. Chan, *Nature Communications* **2023** 14:1 **14**, 1 (2023).
- [69] M. Motta, K. J. Sung, K. B. Whaley, M. Head-Gordon, and J. Shee, *Chemical Science* **14**, 11213 (2023).
- [70] C. Gidney, N. Shutty, and C. Jones, (2024), [arXiv:2409.17595 \[quant-ph\]](#).
- [71] D. Litinski, *Quantum* **3**, 128 (2019).
- [72] Y. Akahoshi, K. Maruyama, H. Oshima, S. Sato, and K. Fujii, *PRX Quantum* **5**, 010337 (2024).
- [73] Z. Ding and L. Lin, *Quantum* **7**, 1136 (2023).
- [74] F. Verstraete, J. I. Cirac, and J. I. Latorre, *Phys. Rev. A* **79**, 032316 (2009).
- [75] L. Bassman Oftelie, R. Van Beeumen, E. Younis, E. Smith, C. Iancu, and W. A. de Jong, *Materials Theory* **6**, 13 (2022).
- [76] A. Schubert and C. B. Mendl, *Phys. Rev. B* **108**, 195105 (2023).
- [77] Y. R. Sanders, D. W. Berry, P. C. Costa, L. W. Tessler, N. Wiebe, C. Gidney, H. Neven, and R. Babbush, *PRX Quantum* **1**, 020312 (2020).

Appendix A: Time evolution of Tile Hamiltonians

This appendix describes how to diagonalize and perform time evolution of tile Hamiltonians for four examples of tiles: S_1 , S_2 , C_4 and S_4 . The Hamiltonian of a tile is defined as

$$H_\sigma^{\text{tile}} = -\tau \sum_{ij} R_{ij}^{\text{tile}} a_{i\sigma}^\dagger a_{j\sigma}, \quad (\text{A1})$$

where R^{tile} is the adjacency matrix describing the nearest-neighbor hopping interactions contained in the tile Hamiltonian, meaning $R_{ij}^{\text{tile}} = 1$ if the tile Hamiltonian contains a hopping term between site i and j , and otherwise $R_{ij}^{\text{tile}} = 0$. The time evolution operator can be implemented as

$$e^{-iH_\sigma^{\text{tile}}t} = e^{i\tau \sum_{ij} R_{ij}^{\text{tile}} a_{i\sigma}^\dagger a_{j\sigma}t} = e^{i\tau M_\sigma^{\text{tile}}t}, \quad (\text{A2})$$

where M_σ^{tile} is defined as

$$M_\sigma^{\text{tile}} = \sum_{ij} R_{ij}^{\text{tile}} a_{i\sigma}^\dagger a_{j\sigma}. \quad (\text{A3})$$

Since the adjacency matrix, R^{tile} , is real symmetric, it has real eigenvalues, λ_e , and eigenvectors, v_e , and it can be diagonalized as $R^{\text{tile}} = \sum_e \lambda_e v_e^\dagger v_e$. Thus,

$$M_\sigma^{\text{tile}} = \sum_{ij} \sum_e \lambda_e (v_e)_i (v_e)_j a_{i\sigma}^\dagger a_{j\sigma}, \quad (\text{A4})$$

$$= \sum_e \lambda_e \left(\sum_i (v_e)_i a_{i\sigma}^\dagger \right) \left(\sum_j (v_e)_j a_{j\sigma} \right), \quad (\text{A5})$$

$$= \sum_e \lambda_e b_e^\dagger b_e, \quad (\text{A6})$$

for $b_e = \sum_j (v_e)_j a_{j\sigma}$, where $(v_e)_j$ is the j 'th element of eigenvector v_e . Whenever an eigenvalue λ_e equals 0, this decomposition will reduce the number of required arbitrary rotations. Throughout this section, we only focus on the eigenvectors that have non-zero eigenvalues.

The tile Hamiltonians considered here contain hopping terms corresponding to star or circle interaction graphs of type S_{2^n} or C_{2^n} , where the subscript denotes the number of edges and n is an integer. Fig. 4(a) shows four tiles of this type: S_1 , S_2 , plaquette (C_4) and S_4 . These tiles can be used to cover arbitrary lattices in order to divide the lattices into sections that can be efficiently diagonalized. There exist other tiles of type S_{2^n} or C_{2^n} that can be used for Tile Trotterization, but the four tiles given in Fig. 4(a) are sufficient for most practical purposes.

The tile Hamiltonians are diagonalized using the fermionic operator F_{ij} [21, 74]. We let F_{ij} act on creation and annihilation operators defined in a two-spin-orbital subspace as

$$F_{ij} a_{i\sigma} F_{ij}^\dagger = \frac{1}{\sqrt{2}} (a_{i\sigma} + a_{j\sigma}), \quad (\text{A7})$$

$$F_{ij} a_{j\sigma} F_{ij}^\dagger = \frac{1}{\sqrt{2}} (a_{i\sigma} - a_{j\sigma}). \quad (\text{A8})$$

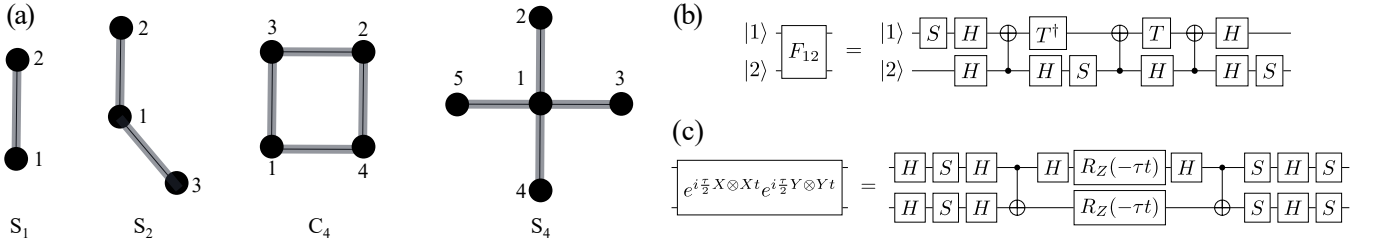


FIG. 4. (a) Illustrations of the four tiles considered in this paper: S_1 , S_2 , C_4 and S_4 . Each lattice site is indexed with a number that corresponds to the order of the spin orbitals in the JW-string, and the edges represents nearest-neighbor hopping interactions between neighboring lattice sites. (b) Quantum circuit diagram for implementing fermionic operator F_{ij} , which is shown through the implementation of F_{12} on a two-qubit subspace, in the Jordan-Wigner representation. (c) Quantum circuit diagram for implementing $e^{i\frac{\tau}{2}X\otimes Xt}e^{i\frac{\tau}{2}Y\otimes Yt}$, up to a global phase.

These examples are given for annihilation operators and can be trivially extended to creation operators. Under the Jordan-Wigner (JW) transformation, the qubit representation of F_{ij} acting on neighboring fermions i and j in the JW string is given by [21]

$$F_{ij} = \begin{pmatrix} 1 & 0 & 0 & 0 \\ 0 & \frac{1}{\sqrt{2}} & \frac{1}{\sqrt{2}} & 0 \\ 0 & \frac{1}{\sqrt{2}} & -\frac{1}{\sqrt{2}} & 0 \\ 0 & 0 & 0 & -1 \end{pmatrix}, \quad (\text{A9})$$

which can be implemented using just 2 T gates with the quantum circuit given in Fig. 4(b) [20].

The qubit implementation of fermionic operators under the JW transformation requires keeping track of the anti-symmetric fermionic properties during the computation. The qubit implementation of F_{ij} is non-local in the JW string ordering, such that implementing F_{ij} on non-adjacent qubits in the JW ordering would introduce additional complexity. This can be solved by using fermionic swap gates to update the JW ordering as needed, so that F_{ij} is only applied on adjacent qubits. The qubit representation of the fermionic swap gate is given by [20]

$$f_{\text{swap}} = \begin{pmatrix} 1 & 0 & 0 & 0 \\ 0 & 0 & 1 & 0 \\ 0 & 1 & 0 & 0 \\ 0 & 0 & 0 & -1 \end{pmatrix}, \quad (\text{A10})$$

which can be implemented using a SWAP gate followed by a CZ gate, having Clifford cost only.

In our costing of $e^{-iH_{\sigma}^{\text{tile}}t}$, we assume an initial JW ordering constructed to avoid using (or in the case of the S_4 tile, to minimize) fermionic swap gates when diagonalizing a tile Hamiltonian. The initial JW ordering within a given tile follow the labels of the sites given in Fig. 4(a). In general, the Clifford costings for implementing time evolution of the tile Hamiltonian depend on the initial JW ordering of the qubits used.

It is also important to note that different hopping sections will require different JW orderings. Therefore, in a full implementation we would require layers of f_{swap} gates in between sections, but we do not account for this Clifford only cost in this paper.

The rest of Appendix A will show how to diagonalize the tile Hamiltonians and provide quantum circuits for implementing $e^{-iH_{\sigma}^{\text{tile}}t}$ for the S_1 , S_2 , C_4 and S_4 tiles. We provide non-Clifford and Clifford gate counts for the implementation of each $e^{-iH_{\sigma}^{\text{tile}}t}$, and the cost of these are summarized in Table I.

1. S_1 tile

The S_1 tile has hopping terms between two spin orbitals $\phi_{1\sigma}$ and $\phi_{2\sigma}$, and contains hopping terms encoded by the adjacency matrix

$$R^{S_1} = \begin{pmatrix} 0 & 1 \\ 1 & 0 \end{pmatrix}, \quad (\text{A11})$$

with eigenvalues $\lambda_+ = 1$ and $\lambda_- = -1$ and corresponding eigenvectors

$$v_+ = \begin{pmatrix} 1/\sqrt{2} \\ 1/\sqrt{2} \end{pmatrix}, \quad v_- = \begin{pmatrix} 1/\sqrt{2} \\ -1/\sqrt{2} \end{pmatrix}. \quad (\text{A12})$$

Therefore, $M_{\sigma}^{S_1}$ can be written as

$$M_{\sigma}^{S_1} = b^{\dagger}b - c^{\dagger}c, \quad (\text{A13})$$

where b and c are given by

$$b = \frac{1}{\sqrt{2}}(a_{1\sigma} + a_{2\sigma}), \quad (\text{A14})$$

$$c = \frac{1}{\sqrt{2}}(a_{1\sigma} - a_{2\sigma}). \quad (\text{A15})$$

Employing the unitary transformation $V = F_{12}$, we can write

$$b = Va_{1\sigma}V^{\dagger}, \quad (\text{A16})$$

$$c = Va_{2\sigma}V^{\dagger}, \quad (\text{A17})$$

and we can implement the time evolution of the S_1 tile on $|\phi_{1\sigma}\phi_{2\sigma}\rangle$, as

$$e^{-iH^{S_1}t} = Ve^{i\tau(a_{1\sigma}^{\dagger}a_{1\sigma} - a_{2\sigma}^{\dagger}a_{2\sigma})t}V^{\dagger}. \quad (\text{A18})$$

Tile	Arbitrary rotations	T gates	CNOT gates	Hadamard gates	S gates	f_{swap}
S_1	2	0	2	8	6	0
S_2	2	4	8	20	12	0
C_4	2	8	14	32	18	0
S_4	2	12	20	44	24	2

TABLE I. The cost for implementing $e^{-iH_\sigma^{\text{tile}}t}$ for S_1 , S_2 , C_4 and S_4 tiles, assuming an initial JW-ordering of spin orbitals given in Fig. 4(a). Note that these tiles require two arbitrary rotations each while the other gate costs scale with the size of the tile. To obtain the cost, we assume an F_{ij} implementation using the quantum circuit in Fig. 4(b) and an implementation of $e^{iX \otimes X \theta} e^{iY \otimes Y \theta}$, where θ is a parameter dependent on τ and t , using the quantum circuit in Fig. 4(c). Further optimization of the Clifford gate costs could be performed, for example by merging gates from F_{ij} with gates from $e^{iX \otimes X \theta} e^{iY \otimes Y \theta}$.

Under the Jordan-Wigner transformation, we can write

$$e^{i\tau(a_{1\sigma}^\dagger a_{1\sigma} - a_{2\sigma}^\dagger a_{2\sigma})t} = \begin{pmatrix} 1 & 0 & 0 & 0 \\ 0 & e^{i\tau t} & 0 & 0 \\ 0 & 0 & e^{-i\tau t} & 0 \\ 0 & 0 & 0 & 1 \end{pmatrix}, \quad (\text{A19})$$

which means Eq. A18 can be further compiled to

$$e^{-iH^{S_1}t} = F_{12} e^{i\tau(a_{1\sigma}^\dagger a_{1\sigma} - a_{2\sigma}^\dagger a_{2\sigma})t} F_{12}^\dagger = \begin{pmatrix} 1 & 0 & 0 & 0 \\ 0 & \cos(\tau t) & i \sin(\tau t) & 0 \\ 0 & i \sin(\tau t) & \cos(\tau t) & 0 \\ 0 & 0 & 0 & 1 \end{pmatrix} = e^{i\frac{\tau}{2} X \otimes X t} e^{i\frac{\tau}{2} Y \otimes Y t}. \quad (\text{A20})$$

This operation can be implemented using the quantum circuit given in Fig. 4(c), which can be found in Eq. 18 of Ref. [75] using $\theta_1 = \theta_2 = -\tau t$.

The total non-Clifford gate count for implementing $e^{-iH^{S_1}t}$ is 2 arbitrary rotations of the same angle. This implementation also requires 2 CNOT gates, 6 S gates and 8 Hadamard gates.

2. S_2 tile

The S_2 tile has hopping terms between three spin orbitals $\phi_{1\sigma}$, $\phi_{2\sigma}$ and $\phi_{3\sigma}$, described by the adjacency matrix

$$R^{S_2} = \begin{pmatrix} 0 & 1 & 1 \\ 1 & 0 & 0 \\ 1 & 0 & 0 \end{pmatrix}, \quad (\text{A21})$$

with eigenvalues $\lambda_0 = 0$, $\lambda_+ = \sqrt{2}$ and $\lambda_- = -\sqrt{2}$ and corresponding eigenvectors

$$v_+ = \begin{pmatrix} 1/\sqrt{2} \\ 1/2 \\ 1/2 \end{pmatrix}, \quad v_- = \begin{pmatrix} 1/\sqrt{2} \\ -1/2 \\ -1/2 \end{pmatrix}. \quad (\text{A22})$$

Therefore $M_\sigma^{S_2}$ can be written as

$$M_\sigma^{S_2} = \sqrt{2} b^\dagger b - \sqrt{2} c^\dagger c, \quad (\text{A23})$$

where b and c are given by

$$b = \frac{1}{\sqrt{2}} a_{1\sigma} + \frac{1}{2} (a_{2\sigma} + a_{3\sigma}), \quad (\text{A24})$$

$$c = \frac{1}{\sqrt{2}} a_{1\sigma} - \frac{1}{2} (a_{2\sigma} + a_{3\sigma}). \quad (\text{A25})$$

Employing the unitary transformation $V = F_{23} F_{12}$, we can write

$$b = V a_{1\sigma} V^\dagger, \quad (\text{A26})$$

$$c = V a_{2\sigma} V^\dagger, \quad (\text{A27})$$

and so can implement the time evolution of the S_2 tile on $|\phi_{1\sigma} \phi_{2\sigma} \phi_{3\sigma}\rangle$ as

$$e^{-iH^{S_2}t} = V e^{i\tau\sqrt{2}(a_{1\sigma}^\dagger a_{1\sigma} - a_{2\sigma}^\dagger a_{2\sigma})t} V^\dagger. \quad (\text{A28})$$

This can be further compiled using

$$F_{12} e^{i\tau\sqrt{2}(a_{1\sigma}^\dagger a_{1\sigma} - a_{2\sigma}^\dagger a_{2\sigma})t} F_{12}^\dagger = \begin{pmatrix} 1 & 0 & 0 & 0 \\ 0 & \cos(\sqrt{2}\tau t) & i \sin(\sqrt{2}\tau t) & 0 \\ 0 & i \sin(\sqrt{2}\tau t) & \cos(\sqrt{2}\tau t) & 0 \\ 0 & 0 & 0 & 1 \end{pmatrix} = e^{i\frac{\tau}{\sqrt{2}} X \otimes X t} e^{i\frac{\tau}{\sqrt{2}} Y \otimes Y t}, \quad (\text{A29})$$

leading to the final expression

$$e^{-iH_\sigma^{S_2}t} = F_{23} e^{i\frac{\tau}{\sqrt{2}} X_1 \otimes X_2 t} e^{i\frac{\tau}{\sqrt{2}} Y_1 \otimes Y_2 t} F_{23}^\dagger. \quad (\text{A30})$$

The total gate cost for implementing the time evolution of the S_2 tile Hamiltonian is therefore two arbitrary rotations, 4 T gates, 8 CNOT gates, 12 S gates and 20 Hadamard gates.

3. C_4 tile

The plaquette (C_4) tile, which first introduced in Ref. [21], has hopping terms between four spin orbitals, $\phi_{1\sigma}$, $\phi_{2\sigma}$, $\phi_{3\sigma}$ and $\phi_{4\sigma}$. It can be described by the adjacency matrix

$$R^{C_4} = \begin{pmatrix} 0 & 0 & 1 & 1 \\ 0 & 0 & 1 & 1 \\ 1 & 1 & 0 & 0 \\ 1 & 1 & 0 & 0 \end{pmatrix}, \quad (\text{A31})$$

for the Jordan-Wigner string ordering $|\phi_{1\sigma}\phi_{2\sigma}\phi_{3\sigma}\phi_{4\sigma}\rangle$ following the site labels given in Fig. 4(a). This adjacency matrix has two zero eigenvalues, $\lambda_+ = 2$ and $\lambda_- = -2$ and corresponding eigenvectors

$$v_+ = \frac{1}{2} \begin{pmatrix} 1 \\ 1 \\ 1 \\ 1 \end{pmatrix}, \quad v_- = \frac{1}{2} \begin{pmatrix} 1 \\ 1 \\ -1 \\ -1 \end{pmatrix}. \quad (\text{A32})$$

Therefore $M_\sigma^{C_4}$ can be written as

$$M_\sigma^{C_4} = 2b^\dagger b - 2c^\dagger c, \quad (\text{A33})$$

where b and c are given by

$$b = \frac{1}{2}(a_{1\sigma} + a_{2\sigma} + a_{3\sigma} + a_{4\sigma}), \quad (\text{A34})$$

$$c = \frac{1}{2}(a_{1\sigma} + a_{2\sigma} - a_{3\sigma} - a_{4\sigma}). \quad (\text{A35})$$

Employing the unitary transformation $V = F_{34}F_{21}F_{23}$, we can write

$$b = Va_{2\sigma}V^\dagger, \quad (\text{A36})$$

$$c = Va_{3\sigma}V^\dagger, \quad (\text{A37})$$

and can implement the time evolution as

$$e^{-iH_\sigma^{C_4}t} = Ve^{i\tau 2(a_{2\sigma}^\dagger a_{2\sigma} - a_{3\sigma}^\dagger a_{3\sigma})t}V^\dagger. \quad (\text{A38})$$

This can be further compiled using

$$F_{23}e^{i\tau 2(a_{2\sigma}^\dagger a_{2\sigma} - a_{3\sigma}^\dagger a_{3\sigma})t}F_{23}^\dagger = \begin{pmatrix} 1 & 0 & 0 & 0 \\ 0 & \cos(2\tau t) & i \sin(2\tau t) & 0 \\ 0 & i \sin(2\tau t) & \cos(2\tau t) & 0 \\ 0 & 0 & 0 & 1 \end{pmatrix} = e^{i\tau X \otimes X t} e^{i\tau Y \otimes Y t}. \quad (\text{A39})$$

The time evolution of the C_4 tile Hamiltonian can then be implemented as

$$e^{-iH_\sigma^{C_4}t} = F_{34}F_{21}e^{i\tau X_2 \otimes X_3 t} e^{i\tau Y_2 \otimes Y_3 t} F_{21}^\dagger F_{34}^\dagger, \quad (\text{A40})$$

which requires 2 arbitrary rotations and 8 T gates. The total gate cost for implementing the time evolution of the C_4 tile Hamiltonian is summarized in Table I.

4. S_4 tile

The S_4 tile has hopping terms between 5 spin orbitals, $\phi_{1\sigma}$, $\phi_{2\sigma}$, $\phi_{3\sigma}$, $\phi_{4\sigma}$ and $\phi_{5\sigma}$, described by the adjacency

matrix

$$R^{S_4} = \begin{pmatrix} 0 & 1 & 1 & 1 & 1 \\ 1 & 0 & 0 & 0 & 0 \\ 1 & 0 & 0 & 0 & 0 \\ 1 & 0 & 0 & 0 & 0 \\ 1 & 0 & 0 & 0 & 0 \end{pmatrix}. \quad (\text{A41})$$

This matrix has three zero eigenvalues, $\lambda_+ = 2$ and $\lambda_- = -2$ and corresponding eigenvectors

$$v_+ = \begin{pmatrix} 1/\sqrt{2} \\ 1/(2\sqrt{2}) \\ 1/(2\sqrt{2}) \\ 1/(2\sqrt{2}) \\ 1/(2\sqrt{2}) \end{pmatrix}, \quad v_- = \begin{pmatrix} 1/\sqrt{2} \\ -1/(2\sqrt{2}) \\ -1/(2\sqrt{2}) \\ -1/(2\sqrt{2}) \\ -1/(2\sqrt{2}) \end{pmatrix}. \quad (\text{A42})$$

This means $M_\sigma^{S_4}$ can be written as

$$M_\sigma^{S_4} = 2b^\dagger b - 2c^\dagger c, \quad (\text{A43})$$

where b and c are given by

$$b = \frac{1}{\sqrt{2}} \left(a_{1\sigma} + \frac{1}{2}(a_{2\sigma} + a_{3\sigma} + a_{4\sigma} + a_{5\sigma}) \right), \quad (\text{A44})$$

$$c = \frac{1}{\sqrt{2}} \left(a_{1\sigma} - \frac{1}{2}(a_{2\sigma} + a_{3\sigma} + a_{4\sigma} + a_{5\sigma}) \right). \quad (\text{A45})$$

Employing the unitary transformation $V = F_{45}F_{32}F_{34}f_{\text{swap}}^{23}F_{13}$, we can write

$$b = Va_{1\sigma}V^\dagger, \quad (\text{A46})$$

$$c = Va_{3\sigma}V^\dagger, \quad (\text{A47})$$

where f_{swap}^{23} is the fermionic swap operator that swaps the electrons in orbitals 2 and 3, such that the orbitals $\phi_{1\sigma}$ and $\phi_{3\sigma}$ adjacent in the Jordan-Wigner ordering after the swap performed by V^\dagger . The following f_{swap}^{23} in V returns the orbitals to the initial JW-ordering.

The time evolution of the S_4 tile Hamiltonian can therefore be implemented on $|\phi_{1\sigma}\phi_{2\sigma}\phi_{3\sigma}\phi_{4\sigma}\phi_{5\sigma}\rangle$ as

$$e^{-iH_\sigma^{S_4}t} = Ve^{i\tau 2(a_{1\sigma}^\dagger a_{1\sigma} - a_{2\sigma}^\dagger a_{2\sigma})t}V^\dagger. \quad (\text{A48})$$

This can be further compiled using (remember that ϕ_1 and ϕ_3 are adjacent after the swap)

$$F_{13}e^{i\tau 2(a_{1\sigma}^\dagger a_{1\sigma} - a_{3\sigma}^\dagger a_{3\sigma})t}F_{13}^\dagger = \begin{pmatrix} 1 & 0 & 0 & 0 \\ 0 & \cos(2\tau t) & i \sin(2\tau t) & 0 \\ 0 & i \sin(2\tau t) & \cos(2\tau t) & 0 \\ 0 & 0 & 0 & 1 \end{pmatrix} = e^{i\tau X \otimes X t} e^{i\tau Y \otimes Y t}, \quad (\text{A49})$$

resulting in the following expression for the time evolution of the S_4 tile Hamiltonian,

$$e^{-iH_\sigma^{S_4}t} = F_{45}F_{32}F_{34}f_{\text{swap}}^{23}e^{i\tau X_1 \otimes X_3 t} e^{i\tau Y_1 \otimes Y_3 t} \times f_{\text{swap}}^{23}F_{34}^\dagger F_{32}^\dagger F_{45}^\dagger, \quad (\text{A50})$$

which requires 2 arbitrary rotations and 12 T gates. The total gate cost for implementing time evolution of the S_4 tile Hamiltonian is summarized in Table I

Appendix B: Tile Trotterization decomposition

Here, we show that the Trotter error norm of Tile Trotterization can be obtained as $W_{\text{tile}} \leq W_{\text{SO}_2} + W_h$, given that we can compute W_{SO_2} and W_h that come from the following Trotter partitionings:

$$\left\| e^{-i(H_h+H_C)t} - e^{-iH_C t/2} e^{-iH_h t} e^{-iH_C t/2} \right\| \leq W_{\text{SO}_2} t^3, \quad (\text{B1})$$

$$\left\| e^{-iH_h t} - \prod_{s=1}^S e^{-iH_h^s t/2} \prod_{s=S}^1 e^{-iH_h^s t/2} \right\| \leq W_h t^3. \quad (\text{B2})$$

The Tile Trotterization error norm, W_{tile} , can be calculated as

$$\left\| e^{-iHt} - e^{-iH_C \frac{t}{2}} \prod_{s=1}^S e^{-iH_h^s \frac{t}{2}} \prod_{s=S}^1 e^{-iH_h^s \frac{t}{2}} e^{-iH_C \frac{t}{2}} \right\| \leq W_{\text{tile}} t^3 \leq (W_{\text{SO}_2} + W_h) t^3, \quad (\text{B3})$$

which is shown by the following derivation:

$$\left\| e^{-i(H_h+H_C)t} - e^{-iH_C t/2} \prod_{s=1}^S e^{-iH_h^s t/2} \prod_{s=S}^1 e^{-iH_h^s t/2} e^{-iH_C t/2} \right\| \quad (\text{B4})$$

$$= \left\| e^{-i(H_h+H_C)t} - e^{-iH_C t/2} e^{-iH_h t} e^{-iH_C t/2} + e^{-iH_C t/2} e^{-iH_h t} e^{-iH_C t/2} - e^{-iH_C t/2} \prod_{s=1}^S e^{-iH_h^s t/2} \prod_{s=S}^1 e^{-iH_h^s t/2} e^{-iH_C t/2} \right\| \quad (\text{B5})$$

$$\leq \left\| e^{-i(H_h+H_C)t} - e^{-iH_C t/2} e^{-iH_h t} e^{-iH_C t/2} \right\| + \left\| e^{-iH_C t/2} e^{-iH_h t} e^{-iH_C t/2} - e^{-iH_C t/2} \prod_{s=1}^S e^{-iH_h^s t/2} \prod_{s=S}^1 e^{-iH_h^s t/2} e^{-iH_C t/2} \right\| \quad (\text{B6})$$

$$\leq W_{\text{SO}_2} t^3 + \left\| e^{-iH_C t/2} \left(e^{-iH_h t} - \prod_{s=1}^S e^{-iH_h^s t/2} \prod_{s=S}^1 e^{-iH_h^s t/2} \right) e^{-iH_C t/2} \right\|, \quad (\text{B7})$$

$$\leq W_{\text{SO}_2} t^3 + \left\| e^{-iH_C t/2} \left\| \left(e^{-iH_h t} - \prod_{s=1}^S e^{-iH_h^s t/2} \prod_{s=S}^1 e^{-iH_h^s t/2} \right) \right\| e^{-iH_C t/2} \right\|, \quad (\text{B8})$$

$$\leq (W_{\text{SO}_2} + W_h) t^3. \quad (\text{B9})$$

Therefore the Tile Trotterization error norm can be bounded by a sum of the more simple error norms, W_{SO_2} and W_h .

Appendix C: An expression for the hopping Hamiltonian Trotter error norm W_h

Tile Trotterization splits the hopping Hamiltonian into S sections and uses the following Trotter decomposition to implement the hopping Hamiltonian,

$$\left\| e^{-iH_h t} - \prod_{s=1}^S e^{-iH_h^s t/2} \prod_{s=S}^1 e^{-iH_h^s t/2} \right\| \leq W_h t^3. \quad (\text{C1})$$

In the case where it is possible to divide a lattice into three sections of colors blue, red and gold, we have that $S = 3$ and that the hopping Hamiltonian sections can be written as $H_1 = H_h^b$, $H_2 = H_h^r$ and $H_3 = H_h^g$, where the subscripts 1, 2 and 3 imply the order in which the terms are implemented within the Trotter step.

The Trotter error norm, W_h , can be obtained from Eq. (15), which can be written out using using a package provided by Schubert *et al.* [76], which automatically writes out Eq. (15) for an arbitrary number of non-commuting Hamiltonian terms. We evaluate Eq. (15) for $H_1 = H_h^b$, $H_2 = H_h^r$ and $H_3 = H_h^g$ as

$$\begin{aligned} W_h &= \frac{1}{12} \left(\left\| [[H_h^b, H_h^r], H_h^r] \right\| + \left\| [[H_h^b, H_h^r], H_h^g] \right\| + \left\| [[H_h^b, H_h^g], H_h^r] \right\| + \left\| [[H_h^b, H_h^g], H_h^g] \right\| + \left\| [[H_h^r, H_h^g], H_h^g] \right\| \right) \\ &+ \frac{1}{24} \left(\left\| [[H_h^b, H_h^r], H_h^b] \right\| + \left\| [[H_h^b, H_h^g], H_h^b] \right\| + \left\| [[H_h^r, H_h^g], H_h^r] \right\| \right). \end{aligned} \quad (\text{C2})$$

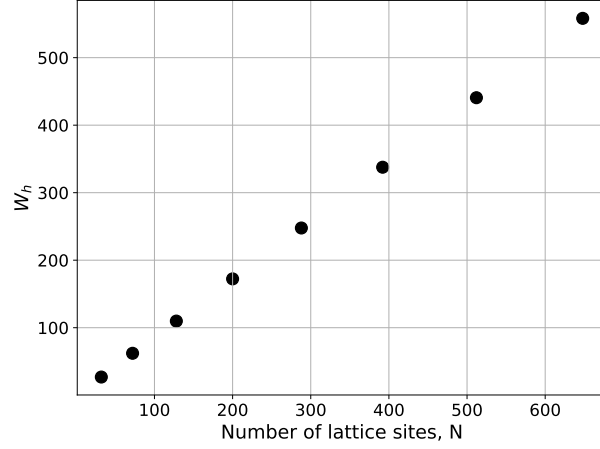


FIG. 5. The hopping Hamiltonian Trotter error norm, W_h , as a function of the number of lattice sites, N , for the periodic hexagonal lattice, using the division described in Appendix D.

This expression can be evaluated from the adjacency matrices of the different sections. The Hamiltonian sections can be written as

$$H_h^b = -\tau \sum_{ij\sigma} R_{ij}^b a_{i\sigma}^\dagger a_{j\sigma}, \quad (\text{C3})$$

$$H_h^r = -\tau \sum_{ij\sigma} R_{ij}^r a_{i\sigma}^\dagger a_{j\sigma}, \quad (\text{C4})$$

$$H_h^g = -\tau \sum_{ij\sigma} R_{ij}^g a_{i\sigma}^\dagger a_{j\sigma}, \quad (\text{C5})$$

where R^r , R^b and R^g are the adjacency matrices of the red, blue and gold lattice sections respectively. Because the Hamiltonian section operators are free fermionic, and using the argument of Ref. [21] Appendix A, this expression for W_h can be evaluated from the adjacency matrices as

$$W_h = \frac{\tau^3}{12} \left(\|[[R^b, R^r], R^r]\|_1 + \|[[R^b, R^r], R^g]\|_1 + \|[[R^b, R^g], R^r]\|_1 + \|[[R^b, R^g], R^g]\|_1 + \|[[R^r, R^g], R^g]\|_1 \right) + \frac{\tau^3}{24} \left(\|[[R^b, R^r], R^b]\|_1 + \|[[R^b, R^g], R^b]\|_1 + \|[[R^r, R^g], R^r]\|_1 \right), \quad (\text{C6})$$

where $\|\cdot\|_1$ is the Schatten one-norm and τ is the hopping parameter. This expression can be used to evaluate W_h for any model where the lattice can be divided into three lattice sections.

The hopping section error norm, W_h , is evaluated numerically for the periodic hexagonal lattice using the lattice division described in Appendix D, and scales linearly in N . This is shown in Fig. 5 for a lattice with parameters $L_x = L_y = L$ in the range $4 \leq L \leq 18$ for even L and hopping parameter $\tau = 1$. This figure shows W_h as a function of the number of lattice sites N , demonstrating the linear dependence in the given range of L .

Appendix D: Periodic Hexagonal lattice model

We consider the periodic hexagonal lattice model shown in Fig. 6(a). Each lattice point pair of color white and grey are labeled by (l_x, l_y) which is defined from the (x, y) positions of the lattice pairs as: $(x, y) = (a \cdot l_x, b \cdot l_y)$, where a and b are the lattice vectors. We define the dimension of the lattice as $L_x = \max(l_x) + 1$ and $L_y = \max(l_y) + 1$, such that the number of lattice sites is $N = 2L_x L_y$. When providing numerical results, we only consider hexagonal lattice models with param-

eters $L_x = L_y = L$ in the range $4 \leq L \leq 18$ for even L .

All lattices, both periodic and non-periodic, can be divided into sections in a number of different ways using either one type or several different types of tiles. The lattice sections influence both the Trotter error norm, W_h , the parallelizability and the per-Trotter-step gate count. The effect of W_h is however insignificant relative to the total Trotter error norm W_{tile} . Therefore, in order to construct efficient hopping Hamiltonian decompositions we focus on two aspects: 1) minimizing the

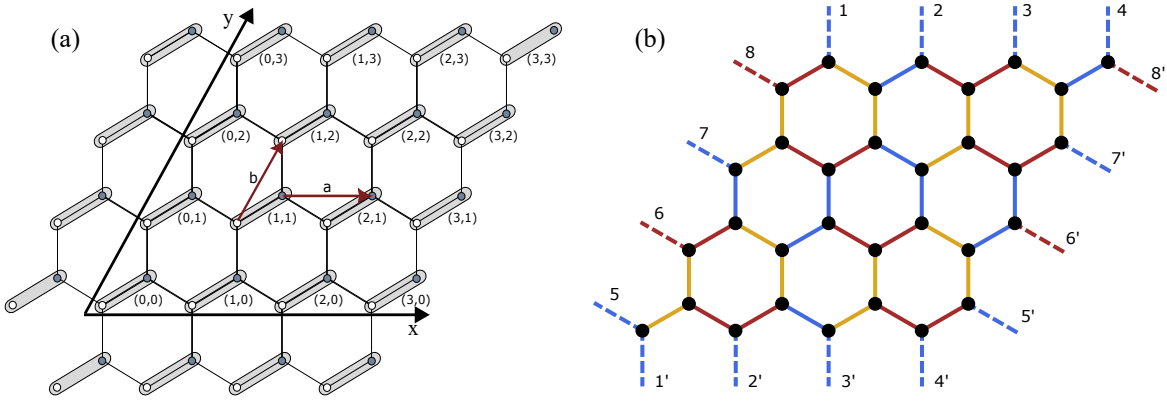


FIG. 6. (a) The periodic hexagonal lattice model where each pair of lattice points are labeled with (l_x, l_y) defined from the (x, y) positions of the lattice points as $(x, y) = (l_x \cdot a, l_y \cdot b)$, where a and b are lattice vectors. The dimension of the lattice is given by $L_x = \max(l_x) + 1$ and $L_y = \max(l_y) + 1$. For this lattice, we have $L_x = L_y = 4$ and $N = 2L_x L_y = 32$. Periodic boundary conditions are applied in the x and y directions which is illustrated through the periodic image in the lattice sketch. (b) The division of a periodic hexagonal lattice with dimensions $L_x = L_y = 4$ into three colored sections: blue, red and gold, using S_2 tiles. The dashed bonds with attached number indicate the bonds that ensure periodicity. For example, the dashed bonds labeled with 1 and 1' indicate the same bond. Each section is covered by $N_b = N_r = N_g = N/4$ S_2 tiles

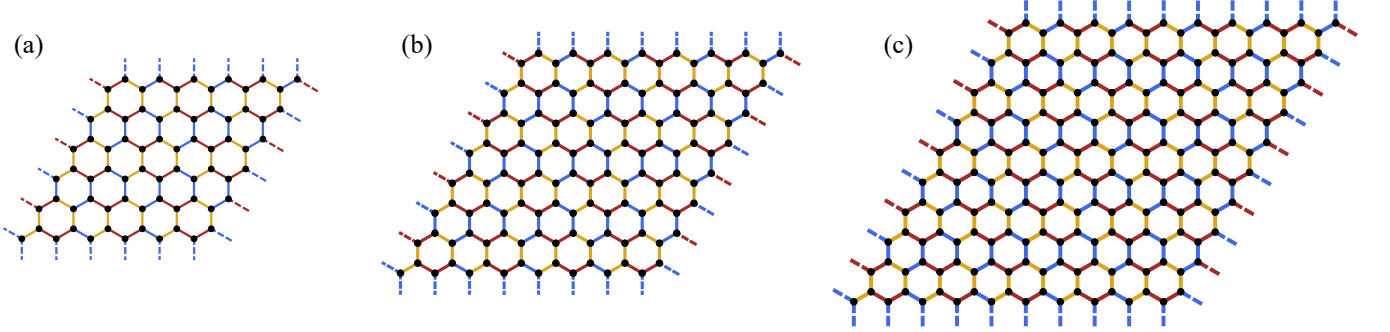


FIG. 7. Illustrations of the periodic hexagonal lattice sections used in this paper for periodic hexagonal lattice models with $L_x = L_y = L$, where the lattices have size parameter (a) $L = 6$, (b) $L = 8$ and (c) $L = 10$, which corresponds to (a) $N = 72$, (b) $N = 128$, (c) $N = 200$. The number of tiles in each section of the periodic hexagonal lattice models is $N_r = N_b = N_g = N/4$ S_2 tiles.

number of sections to improve parallelizability and 2) minimizing the number of tiles in each section to reduce gate counts (assuming we use S_1 , S_2 , C_4 and S_4). These two points are generally not possible to optimize simultaneously. For example, the tiling of the Kagome lattice shown in Fig. 1 can be achieved using more S_4 tiles than the choice demonstrated. This would reduce the overall gate cost of the hopping Hamiltonian but with an additional cost of significantly more sections and reduced parallelizability. Therefore, when choosing efficient tiling of the lattice models, we aim to keep the number of sections to a minimum and try to avoid using S_1 tiles.

We choose to divide our periodic hexagonal lattice models into three sections of colors red, blue and gold using S_2 tiles as shown for $L_x = L_y = 4$ in Fig. 6(b). The dashed bonds with labels 1 and 1' indicate a single bond that ensures periodicity of the lattice. This lattice section division ensures that we have $N_b = N_r = N_g = N/4$ S_2 tiles in each section, which will be the case for all

periodic hexagonal lattice models studied in this paper.

Figs. 7(a-c) show the lattice divisions of the periodic hexagonal lattice model for $L = 6, 8$ and 10 , with a lattice section division following the same structure as for the $L = 4$ case.

Note that it is not a requirement that each section contains the same number of tiles, and in fact this does not necessarily give the most optimal implementation. As shown in Eq. (E1), one Trotter step of hexagonal lattice Hubbard models with three lattice sections uses two applications of $e^{-iH_h^b t/2}$, two applications of $e^{-iH_h^r t/2}$ and one application of $e^{-iH_h^g t}$. Therefore, the gate costings of a Trotter step might be reduced by putting as many tiles as possible into the gold sections while still maintaining the commutativity properties of the gold section. This optimization has not been implemented for the models considered here, but may be considered for concrete future applications in order to take full advantage of the Tile Trotterization method.

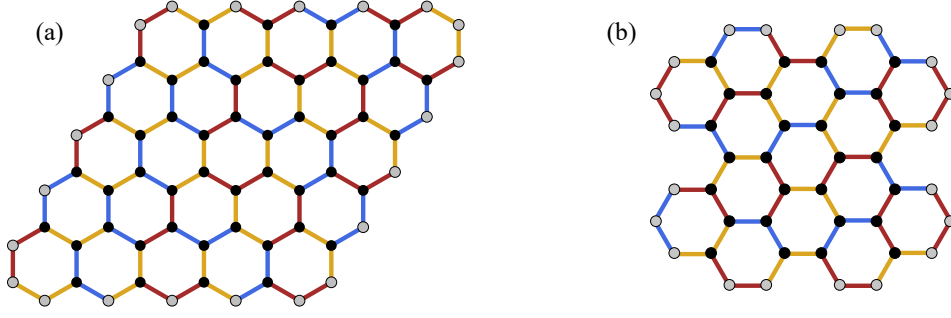


FIG. 8. a) Example of a hexagonal lattice fragment covered by S_2 tiles in three lattice sections with $N_{ed} = 22$ edge sites (gray) and $N_c = 48$ center sites (black). (b) Another example of a hexagonal lattice fragment with a structure inspired by nanographene molecules studied in Ref. [58] which show interesting π -spin properties. This structure is also covered by S_2 tiles in three lattice sections and has $N_{ed} = 20$ edge sites and $N_c = 28$ center sites.

Appendix E: Tile Trotterization applications

In the main text we considered Tile Trotterization of the extended Hubbard model on a periodic hexagonal lattice. Here, we consider the application of Tile Trotterization for three additional systems: the Hubbard model on a non-periodic hexagonal lattice (hexagonal lattice fragments), the periodic hexagonal lattice Hubbard model and the PPP model.

Section E1 shows that Tile Trotterization is applicable also to non-periodic lattice models of arbitrary shapes. For this application, we provide gate counts and Trotter error norms for a specific class of hexagonal lattice fragments. Section E2 presents a simpler version of the main text application and discusses Tile Trotterization of the periodic hexagonal lattice Hubbard model. In our derivation of the gate counts, we consider this periodic model as a special case of the hexagonal lattice fragments in Section E1. The results obtained in Section E2 are used in the quantum phase estimation section of the main text (Section VI) to generate the numerical results used in Figs. 2 and 3(a). Finally, we consider the application of Tile Trotterization for simulating the PPP model in Section E3, but we do not analyze the Trotter error norm for this model.

1. Tile Trotterization of the Hubbard model on hexagonal lattice fragments

We consider all non-periodic hexagonal lattice fragments with the requirement that all lattice sites are part of at least one full hexagon. These fragments have two distinct types of sites: center sites where a lattice site has three nearest neighbors and edge sites where a lattice site has two nearest neighbors. We denote the number of center sites by N_c and the number of edge sites by N_{ed} .

To apply Tile Trotterization, we cover the fragments by S_2 tiles and divide them into three sections of colors: blue (b), red (r) and gold (g). Two examples of fragments and the division into sections are shown in Fig. 8. We

use grey as the color for the edge sites and black as the color for the center sites. Continuing, we use N_b , N_r and N_g as the number of S_2 tiles used in sections b, r and g.

A single Trotter step of the Hubbard model, defined in Eq. (4), on these fragments is implemented as

$$e^{-i(H_h+H_I)t} \approx e^{-iH_I \frac{t}{2}} e^{-iH_h^b \frac{t}{2}} e^{-iH_h^r \frac{t}{2}} e^{-iH_h^g t} \times e^{-iH_h^r \frac{t}{2}} e^{-iH_h^b \frac{t}{2}} e^{-iH_I \frac{t}{2}}, \quad (\text{E1})$$

where we have chosen to implement the sections in the order $H_1 = H_h^b$, $H_2 = H_h^r$ and $H_3 = H_h^g$. Performing r repetitions of this Trotter step gives

$$\left(e^{-i(H_h+H_I)t} \right)^r \approx e^{-iH_I \frac{t}{2}} \left(e^{-iH_h^b \frac{t}{2}} e^{-iH_h^r \frac{t}{2}} e^{-iH_h^g t} e^{-iH_h^r \frac{t}{2}} e^{-iH_h^b \frac{t}{2}} e^{-iH_I t} \right)^r e^{iH_I \frac{t}{2}}, \quad (\text{E2})$$

so that the cost of one Trotter step for large r is two applications of $e^{-iH_h^b t/2}$, two applications of $e^{-iH_h^r t/2}$, one application of $e^{-iH_h^g t}$ and one application of $e^{-iH_I t}$.

Using the Jordan-Wigner transformation, the system is represented by $2N$ qubits and $e^{-iH_I t}$ contains N terms, and can be implemented with one layer of N arbitrary Z-axis rotations of the same angle and two layers of N CNOT gates.

The costing of implementing the time evolution of each hopping section is performed by counting the number of applications of $e^{-iH_{\sigma}^{S_2} t}$ in each section. This Trotter implementation requires $4N_b$, $4N_r$ and $2N_g$ applications of the time evolution operator of the S_2 tile Hamiltonian, accounting for both spin sectors. Only counting the non-Clifford gates, the time evolution of the S_2 tile Hamiltonian can be implemented using two arbitrary Z-axis rotations and 4 T gates as shown in Appendix A. This leads to a total non-Clifford cost per Trotter step of N_R arbitrary rotations and N_T T gates,

$$N_R = N + 8N_b + 8N_r + 4N_g, \quad (\text{E3})$$

$$N_T = 16N_b + 16N_r + 8N_g. \quad (\text{E4})$$

The Tile Trotterization error norm is evaluated as shown in Eq. (22), using W_{SO_2} and W_h . First, we

find an expression for W_{SO_2} from Eq. (24), which shows that we only need to evaluate $\|[[H_I, H_h], H_I]\|$ and $\|[[H_I, H_h], H_h]\|$. These two commutator bounds are given by Lemma 1 and Lemma 2 of Ref. [21]. The first commutator bound is given by

$$\|[[H_I, H_h], H_I]\| \leq U^2 \|H_h\| = U^2 \tau \|R\|_1, \quad (\text{E5})$$

where $\|\cdot\|_1$ is the Schatten one-norm and R is the adjacency matrix of the fragments. The second commutator bound can be evaluated as

$$\|[[H_I, H_h], H_h]\| \leq \frac{U}{2} \sum_i \left(\|T_i, H_h\| + 2\|T_i\|^2 \right), \quad (\text{E6})$$

where T_i is an operator containing all hopping terms that interact with site i . The norm $\|T_i\|$ is only dependent on the character of the specific site i . The fragments have two distinct sites: center and edge sites, therefore $\sum_i 2\|T_i\|^2 = 2\|T_c\|^2 N_c + 2\|T_{ed}\|^2 N_{ed}$. The two norms $\|T_c\|$ and $\|T_{ed}\|$ are evaluated as

$$\|T_c\| = 2\sqrt{3}\tau, \quad (\text{E7})$$

$$\|T_{ed}\| = 2\sqrt{2}\tau, \quad (\text{E8})$$

using the properties of free fermionic operators shown in Appendix F 1 and Eq. (F18), where T_i corresponds to H_k^i with $k = 3$ for the center sites and $k = 2$ for the edge sites.

The norm of the commutator $\|T_i, H_h\|$ is not only dependent on the character of site i but also on neighbor sites of i and can be evaluated for each site i as shown in Eq. (F19) in Appendix F 1. For these models, we find that $\max(\|T_i, H_h\|) = 2\sqrt{6}\tau^2$. The maximum value of the commutator norm is found for the center sites that only has center sites as neighbors. We use this to bound $\sum_i \|T_i, H_h\|$ as

$$\sum_i \|T_i, H_h\| \leq 2\sqrt{6}\tau^2 N, \quad (\text{E9})$$

where the equal sign only holds for periodic hexagonal lattices where all sites have 3 nearest neighbors (with $N_c = N$ and $N_{ed} = 0$).

This leads to the final expression for the second commutator bound

$$\|[[H_I, H_h], H_h]\| \leq U\tau^2 \left(12N_c + 8N_{ed} + \sqrt{6}N \right). \quad (\text{E10})$$

We obtain W_h using Eq. (15) and the order of the hopping sections in the Trotter step: $H_1 = H_h^b$, $H_2 = H_h^r$ and $H_3 = H_h^g$. Eq. (15) is written out for this splitting in Eq. (C2) in Appendix C. Eq. (C6) shows a formula for efficiently calculating W_h for all Tile Trotterization applications where the lattice can be divided into three sections.

2. Tile Trotterization of the Hubbard model on the periodic hexagonal lattice

We use the periodic hexagonal lattice model and the division into sections shown in Figs. 6 and 7, and described in Appendix D. This corresponds to decomposing the hopping Hamiltonian as $H_h = H_h^b + H_h^r + H_h^g$, using $N_b = N_r = N_g = N/4$ S_2 tiles in each section.

A single Trotter step of the Hubbard model on the periodic hexagonal lattice is implemented in the same way as for the arbitrary fragments described in Eqs. (E1)–(E2), so that the cost of one Trotter step (when performing r Trotter steps total) consists of two applications of $e^{-iH_h^b t/2}$, two applications of $e^{-iH_h^r t/2}$, one application of $e^{-iH_h^g t}$ and one application of $e^{-iH_I t}$. Therefore, the cost per Trotter step can again be evaluated as in Eqs. (E3)–(E4), but for the periodic case we can replace the number of tiles in each section by $N/4$, simplifying the non-Clifford cost to

$$N_R = 6N, \quad (\text{E11})$$

$$N_T = 10N. \quad (\text{E12})$$

Arbitrary rotations are expensive to perform on fault-tolerant quantum computers because such operations cannot be protected for arbitrary rotation angles. Hamming weight phasing (HWP) [20, 21, 62] is a method to reduce the number of arbitrary rotations required, which can be applied in the case where many rotations of the same angle are performed in parallel. HWP allows for trading m arbitrary rotations of the same angle with $m - 1$ clean ancilla qubits and $m - 1$ Toffoli gates. The Hubbard model time evolution contains 6 layers of N arbitrary rotations, where the angle of all gates within a given layer are the same. We choose to implement m of these arbitrary rotations simultaneously, where N is an integer multiple of m , which reduces the number of arbitrary rotations per layer to $N_R = \lfloor \log_2(m) + 1 \rfloor$ using $N_{\text{Tof}} = m - 1$ Toffoli gates and $\alpha = m - 1$ clean ancilla qubits. To implement the total amount of $6N$ arbitrary rotations, we need $\frac{6N}{m}$ layers of m arbitrary rotations. This leads to a total gate count per Trotter step of

$$N_R = \frac{6N}{m} \lfloor \log_2(m) + 1 \rfloor, \quad (\text{E13})$$

$$N_{\text{Tof}} = \frac{6N}{m} (m - 1), \quad (\text{E14})$$

$$N_T = 10N. \quad (\text{E15})$$

Each Toffoli gate can be converted into 4 T gates to obtain a total T gate cost of

$$N_T = 10N + 4N_{\text{Tof}} = 10N + 4 \times \frac{6N}{m} (m - 1). \quad (\text{E16})$$

Given that we choose m as a fraction of N , the number of arbitrary rotations per Trotter step scales logarithmically in N and the number of T gates scale linearly in N . The total qubit count needed for this Tile Trotterization implementation is $2N + (m - 1)$.

Note that choosing HWP with $m < N$ reduces the parallelization of arbitrary rotations in each Trotter step because only m arbitrary rotations can be performed simultaneously. Additionally, choosing $m = N$ comes with a significant additional qubit cost so $m = \frac{N}{4}$ or $m = \frac{N}{2}$ might be more advantageous depending on the available resources.

The Tile Trotterization error norm is again evaluated from Eq. (22), and W_{SO_2} is obtained from the commutator bounds given by Lemma 1 and Lemma 2 in Appendix C of Ref. [21]. This leads to the following bounds for the periodic hexagonal lattice

$$\|[[H_I, H_h], H_I]\| \leq U^2 \|H_h\| = U^2 \tau \|R\|_1, \quad (\text{E17})$$

where $\|\cdot\|_1$ is the Schatten one-norm and R is the adjacency matrix of the periodic hexagonal lattice. We note that $\|R\|_1$ has a worst case linear scaling in N . We can bound the second commutator by

$$\begin{aligned} \|[[H_I, H_h], H_h]\| &\leq \frac{U}{2} \sum_i \left(\| [T_i, H_h] \| + 2 \| T_i \|^2 \right) \\ &= (12 + \sqrt{6}) U \tau^2 N, \end{aligned} \quad (\text{E18})$$

using that for all sites i

$$\|T_i\| = 2\sqrt{3}\tau, \quad (\text{E19})$$

$$\|[T_i, H_h]\| = 2\sqrt{6}\tau^2, \quad (\text{E20})$$

which can be evaluated using Eqs. (F18)–(F19) with $H_k^i = H_3^i$. We used the adjacency matrix of the periodic hexagonal lattice model with $L_x = L_y = L = 4$ to evaluate (E20) but the value is independent L .

The lattice is divided into three sections and we can therefore obtain W_h using Eq. (C6) in Appendix C. The hopping Hamiltonian Trotter error norm for the periodic hexagonal lattice division used in this paper scales linearly with N , as shown in Fig. 5. In the numerical examples for the hexagonal lattice periodic Hubbard model given in this paper with $U = 4$ and $\tau = 1$, we find that W_h constitutes around 12.6% of the total Trotter error norm W_{tile} .

Inserting these error bounds into Eq. (22), we find that the Tile Trotterization error norm, W_{tile} , for the periodic hexagonal lattice Hubbard model scales as $\mathcal{O}(N)$.

The results presented in this section are used to obtain the QPE resource estimates for the Hubbard model in Sec. VI, which is used in Fig. 2 and Fig. 3(a).

3. Tile Trotterization of the PPP model on the periodic hexagonal lattice

The strategies for including the nearest-neighbor Coulomb interaction terms as for the extended Hubbard model application can be extended to include even longer range interactions. The PPP model can be used as a model for π -electron systems in conjugated hydrocarbon

molecules, including graphene and nanographene fragments. The PPP model is a Hubbard model Hamiltonian with all-to-all Coulomb interactions, and is therefore the most extreme extension of the electron interaction term in a two-dimensional nearest-neighbor hopping Hubbard model.

We consider the PPP model on the periodic hexagonal lattice shown in Appendix D, with parameters $L_x = L_y = L$. The lattice is therefore covered by $N_b = N_r = N_g = N/4$ S_2 tiles in three sections.

The PPP model contains all-to-all Coulomb interactions such that the potential energy term can be written as

$$H_C = \frac{U}{4} \sum_i Z_{i\uparrow} Z_{i\downarrow} + \frac{1}{8} \sum_{i \neq j} \sum_{\sigma, \sigma'} V_{ij} Z_{i\sigma} Z_{j\sigma'}, \quad (\text{E21})$$

where $Z_{i\sigma} \equiv 2n_{i\sigma} - 1$, U is the on-site interaction strength and V_{ij} represents the interaction strength between electrons in spin orbitals on site i and j . In practice, V_{ij} will depend on the distance between the sites, r_{ij} , as $1/r_{ij}$.

A single Trotter step of the PPP model on the periodic hexagonal lattice can be implemented as

$$\begin{aligned} e^{-i(H_h + H_C)t} &\approx e^{-iH_C \frac{t}{2}} e^{-iH_h^b \frac{t}{2}} e^{-iH_h^r \frac{t}{2}} \\ &\times e^{-iH_h^g t} e^{-iH_h^r \frac{t}{2}} e^{-iH_h^b \frac{t}{2}} e^{-iH_C \frac{t}{2}}, \end{aligned} \quad (\text{E22})$$

where the sections are implemented in the order $H_1 = H_h^b$, $H_2 = H_h^r$ and $H_3 = H_h^g$. Performing r repetitions of this Trotter step gives

$$\begin{aligned} \left(e^{-i(H_h + H_C)t} \right)^r &\approx e^{-iH_C \frac{t}{2}} \left(e^{-iH_h^b \frac{t}{2}} e^{-iH_h^r \frac{t}{2}} e^{-iH_h^g t} \right. \\ &\quad \left. e^{-iH_h^r \frac{t}{2}} e^{-iH_h^b \frac{t}{2}} e^{-iH_C t} \right)^r e^{iH_C \frac{t}{2}} \end{aligned} \quad (\text{E23})$$

so that the cost of one Trotter step for large r is two applications of $e^{-iH_h^b t/2}$, two applications of $e^{-iH_h^r t/2}$, one application of $e^{-iH_h^g t}$ and one application of $e^{-iH_C t}$.

The interaction term H_C contains $\frac{1}{2} \times 4 \times N(N-1) + N = 2N^2 - N$ terms. Meanwhile, the cost of implementing H_h is $5N$ arbitrary rotations and $10N$ T gates as previously discussed for the periodic hexagonal lattice, leading to a total non-Clifford cost of

$$N_R = 2N^2 + 4N, \quad (\text{E24})$$

$$N_T = 10N. \quad (\text{E25})$$

We can also consider grouping the $2N^2 - N$ interaction terms into layers and applying HWP. Applying HWP requires that the rotation angles within a layer are all the same. For completely general V_{ij} values, this will not be the case. However, for physically motivated parameters, V_{ij} depends on the distance between sites i and j . Therefore, we can label the on-site interaction parameter as U , the nearest-neighbor parameter as V_1 , the next-nearest-neighbor parameter as V_2 , and so on. Then, it

will generally be possible to group the $2N^2 - N$ interaction terms into $2N - 1$ layers of N rotations, with the same rotation angles within each layer, so that HWP can be applied to implement $e^{-iH_C t}$. Including the hopping layers, this means that we have to apply $2N + 4$ layers of N arbitrary rotations. Therefore, HWP can be applied efficiently by using $\alpha = N - 1$ ancilla qubits, reducing the cost to

$$N_R = (2N + 4)[\log_2(N) + 1], \quad (\text{E26})$$

$$N_{\text{tof}} = (2N + 4)(N - 1) = 2N^2 + 2N - 4, \quad (\text{E27})$$

$$N_T = 10N. \quad (\text{E28})$$

By implementing each Toffoli gate with 4 T gates, we get

$$N_T = 8N^2 + 18N - 16, \quad (\text{E29})$$

so that the number of T gates in each Trotter step scales as $\mathcal{O}(N^2)$. This implementation of time evolution of the PPP model uses $3N - 1$ qubits.

For such a simulation, the dominant cost inevitably comes from implementing $e^{-iH_C t}$. In practice, it may be possible to reduce the cost of implementing this term, for example, by exploiting the symmetry, which would be an interesting study for future work.

Appendix F: Commutator bounds for the extended Hubbard model

The Tile Trotterization error norm for the extended Hubbard model can be calculated from Eq. (24) as

$$\begin{aligned} W_{\text{SO2}} &\leq \frac{1}{12} \|[[[H_I, H_h], H_h]]\| \\ &+ \frac{1}{12} \|[[[H_V, H_h], H_h]]\| \\ &+ \frac{1}{24} \|[[[H_I + H_V, H_h], H_I + H_V]]\|, \end{aligned} \quad (\text{F1})$$

where we have used Eq. (34). An expression for $\|[[[H_I, H_h], H_h]]\|$ has already been given in Eq. (E18).

In this section, we find expressions for the remaining commutator bounds $\|[[[H_I + H_V, H_h], H_I + H_V]]\|$ and $\|[[[H_V, H_h], H_h]]\|$. We limit ourselves to lattices where all sites have the same number of nearest neighbors (k -regular graphs), which allows us to use the modified interaction term defined in Eq. (10). We proceed by defining the extended Hubbard model and introduce an alternative way of expressing the model which is used throughout the derivation.

The extended Hubbard model is defined as

$$H_{EH} = H_h + H_I + H_V, \quad (\text{F2})$$

with the Coulomb terms $H_C = H_I + H_V$. The terms are

given by

$$H_h = -\tau \sum_{i,j,\sigma} R_{ij} a_{i\sigma}^\dagger a_{j\sigma}, \quad (\text{F3})$$

$$H_I = \frac{U}{4} \sum_{i=1}^N Z_{i\uparrow} Z_{i\downarrow}, \quad (\text{F4})$$

$$H_V = \frac{V}{8} \sum_{\langle ij \rangle} \sum_{\sigma, \sigma'} Z_{i\sigma} Z_{j\sigma'}. \quad (\text{F5})$$

For $i \neq j$, we define the operator $B_{ij\sigma}$ as the hopping interaction from spin orbital $i\sigma$ to spin orbital $j\sigma$

$$B_{ij\sigma} = -\tau a_{i\sigma}^\dagger a_{j\sigma}, \quad (\text{F6})$$

and define B_{ij} as

$$B_{ij} = B_{ij\uparrow} + B_{ij\downarrow}. \quad (\text{F7})$$

Using this notation, we can write H_h as

$$H_h = \sum_{\langle ij \rangle} B_{ij}, \quad (\text{F8})$$

or as

$$H_h = \frac{1}{2} \sum_{\langle ij \rangle} (B_{ij} + B_{ji}), \quad (\text{F9})$$

where we multiply by $\frac{1}{2}$ to avoid double counting of hopping terms. We let $\sum_{\langle ij \rangle}$ run over kN nearest-neighbor terms for all lattices where each lattice site has k nearest neighbors, and each pair of nearest-neighbor sites (i, j) is included in both orders.

Before evaluating the commutator bounds in Appendices F3 and F4, we show how to compute the operator norm of hopping Hamiltonians that are free fermionic operators in Appendix F1, and then, in Appendix F2, we establish a set of commutator and anti-commutator rules used for the derivations.

1. Operator norm of free fermionic operators

A free fermionic operator can be written as

$$H = \sum_{ij} Q_{ij} a_i^\dagger a_j, \quad (\text{F10})$$

where Q_{ij} is (i, j) entry of a matrix Q that encodes the hopping terms. For free fermionic Hamiltonians with nearest-neighbor hopping interactions, the matrix Q corresponds to an adjacency matrix that encodes the nearest-neighbor hopping terms between the relevant sites i and j . In this paper, we consider hopping Hamiltonians that are divided into two block diagonal spin sectors with

$$Q = \begin{pmatrix} R_\uparrow & 0 \\ 0 & R_\downarrow \end{pmatrix}, \quad (\text{F11})$$

where R_\uparrow is a matrix encoding the hopping terms in the spin-up sector and R_\downarrow is a matrix encoding the hopping terms in the spin-down sector. These matrices are of size $N \times N$ where N is the number of lattice sites.

The operator norm of H can be evaluated as [21]

$$\|H\| = \frac{1}{2}\|Q\|_1 = \frac{1}{2}(\|R_\uparrow\|_1 + \|R_\downarrow\|_1), \quad (\text{F12})$$

where $\|\cdot\|_1$ is the Schatten one-norm. In cases where $R_\uparrow = R_\downarrow = R$, where R is the adjacency matrix of the lattice, the expression simplifies to

$$\|H\| = \|R\|_1. \quad (\text{F13})$$

In some cases, we are interested in only evaluating the norm of hopping interactions in one spin sector. The operator norm of a hopping interaction in spin sector σ can be evaluated as

$$\|H_\sigma\| = \frac{1}{2}\|R_\sigma\|_1. \quad (\text{F14})$$

The same structure applies when evaluating the norm of commutators and nested commutators of free fermionic operators, then

$$\begin{aligned} \|[H_1, H_2]\| &= \frac{1}{2}\|[Q_1, Q_2]\|_1 \\ &= \frac{1}{2}(\|[R_{1\uparrow}, R_{2\uparrow}]\|_1 + \|[R_{1\downarrow}, R_{2\downarrow}]\|_1), \end{aligned} \quad (\text{F15})$$

which can also be used to calculate the norms of commutators in each spin sector.

Below, we provide some concrete examples where we evaluate the norm of relevant free fermionic operators discussed throughout the paper and in the commutator bound derivations.

Given a hopping Hamiltonian of type

$$H_h = -\tau \sum_{i,j,\sigma} R_{ij} a_{i\sigma}^\dagger a_{j\sigma}, \quad (\text{F16})$$

where R is the $N \times N$ adjacency matrix of the hopping interaction in both spin sectors, the operator norm of H_h can be evaluated as

$$\|H_h\| = \tau\|R\|_1. \quad (\text{F17})$$

Consider a hopping operator, H_k^i , that contains hopping terms with parameter τ between sites described by the $N \times N$ adjacency matrix, \tilde{S}_k^i , including both spin sectors. We consider the case where the only non-zero terms of \tilde{S}_k^i are a sub-block corresponding to an S_k star graph located at site i . The star graph \tilde{S}_k^i encodes the hopping terms between site i and its k nearest neighbor sites. Then, the operator norm of H_k^i can be evaluated as

$$\|H_k^i\| = \tau\|\tilde{S}_k^i\|_1 =: \tau\|\tilde{S}_k\|_1. \quad (\text{F18})$$

This norm is in principle dependent on the lattice site i , however we only consider lattices where all sites have the same number of nearest neighbors, k , and therefore we can omit this superscript, as in the final step in Eq. (F18).

Similarly, the operator norm of $[H_k^i, H_h]$ can be evaluated as

$$\|[H_k, H_h]\| = \tau^2\|\tilde{S}_k, R\|_1. \quad (\text{F19})$$

If we are only interested in the operator norm of a single spin sector of H_k^i , we write this as $H_{k,\sigma}^i$, and evaluate the norm as

$$\|H_{k,\sigma}\| = \frac{\tau}{2}\|\tilde{S}_{k,\sigma}\|_1. \quad (\text{F20})$$

The operator norm of the commutator between $H_{k,\sigma}^i$ and H_h can be evaluated as

$$\|[H_{k,\sigma}, H_h]\| = \frac{\tau^2}{2}\|\tilde{S}_{k,\sigma}, R\|_1. \quad (\text{F21})$$

This strategy for finding the operator norm of free fermionic operators is used to evaluate commutator bounds for the specific systems discussed throughout the paper. For more details on computing the norms of free fermionic operators and commutators of free fermionic operators, we refer to Appendix A of Ref. [21].

2. Commutator and anti-commutator rules

In the following derivations, we will need to consider the commutator and anti-commutators between Coloumb terms (of the form $Z_{i\sigma}Z_{j\sigma'}$ for $i\sigma \neq j\sigma'$) and hopping terms (of the form $B_{ij\sigma} = -\tau a_{i\sigma}^\dagger a_{j\sigma}$ for $i \neq j$).

To aid in this task, we establish a set of commutator and anti-commutator rules that are given in Eqs. (F22)–(F25):

$$[Z_{m\sigma_1}Z_{n\sigma_2}, B_{ij\sigma}] = 0 \text{ if spin orbitals } m\sigma_1, n\sigma_2, i\sigma \text{ and } j\sigma \text{ are all different,} \quad (\text{F22})$$

$$[Z_{i\sigma}Z_{j\sigma}, B_{ij\sigma}] = 0, \quad (\text{F23})$$

$$\{Z_{i\sigma}Z_{l\sigma'}, B_{ij\sigma}\} = 0 \text{ if spin orbitals } i\sigma, j\sigma \text{ and } l\sigma' \text{ are all different,} \quad (\text{F24})$$

$$\{Z_{i\sigma}Z_{l\sigma'}, B_{ji\sigma}\} = 0 \text{ if spin orbitals } i\sigma, j\sigma \text{ and } l\sigma' \text{ are all different.} \quad (\text{F25})$$

In words, if the spin orbitals in the Coulomb term are both the same or both different to the spin orbitals in the hopping term, then the *commutator* is zero. In contrast, if one and only one of the spin orbitals is shared between the Coulomb and hopping term, then the *anti-commutator* is zero. This gives the intuition for these results, which we now proceed to derive.

The commutator in Eq. (F22) is trivially true because all operators in the expression act on different spin orbitals. Eqs. (F23) and (F24) can be shown by using the following anti-commutation relation that applies for $\sigma \neq \sigma'$ or $i \neq j$,

$$\{Z_{i\sigma}Z_{j\sigma'}, a_{i\sigma}^\dagger\} = \{(2n_{i\sigma} - \mathbb{1})(2n_{j\sigma'} - \mathbb{1}), a_{i\sigma}^\dagger\} = (2n_{j\sigma'} - \mathbb{1})\{(2n_{i\sigma} - \mathbb{1}), a_{i\sigma}^\dagger\} = 2(2n_{j\sigma'} - \mathbb{1})(\{n_{i\sigma}, a_{i\sigma}^\dagger\} - a_{i\sigma}^\dagger). \quad (\text{F26})$$

This expression can be evaluated by calculating the anti-commutator

$$\{n_{i\sigma}, a_{i\sigma}^\dagger\} = \{a_{i\sigma}^\dagger a_{i\sigma}, a_{i\sigma}^\dagger\} = a_{i\sigma}^\dagger a_{i\sigma} a_{i\sigma}^\dagger + a_{i\sigma}^\dagger a_{i\sigma}^\dagger a_{i\sigma} = a_{i\sigma}^\dagger a_{i\sigma} a_{i\sigma}^\dagger = (\mathbb{1} - a_{i\sigma} a_{i\sigma}^\dagger) a_{i\sigma}^\dagger = a_{i\sigma}^\dagger \quad (\text{F27})$$

using $\{a_{i\sigma}^\dagger, a_{i\sigma}\} = \mathbb{1}$. Inserting this result back into Eq. (F26), we obtain

$$\{Z_{i\sigma}Z_{j\sigma'}, a_{i\sigma}^\dagger\} = 0, \quad (\text{F28})$$

which can also be shown for $a_{i\sigma}$ instead of $a_{i\sigma}^\dagger$ to obtain

$$\{Z_{i\sigma}Z_{j\sigma'}, a_{i\sigma}\} = 0. \quad (\text{F29})$$

Now we can prove Eq. (F23) using the identity $[A, BC] = \{A, B\}C - B\{A, C\}$ and Eqs. (F28)–(F29)

$$[Z_{i\sigma}Z_{j\sigma}, B_{ij\sigma}] = -\tau[Z_{i\sigma}Z_{j\sigma}, a_{i\sigma}^\dagger a_{j\sigma}] = -\tau\left(\{Z_{i\sigma}Z_{j\sigma}, a_{i\sigma}^\dagger\}a_{j\sigma} - a_{i\sigma}^\dagger\{Z_{i\sigma}Z_{j\sigma}, a_{j\sigma}\}\right) = 0. \quad (\text{F30})$$

Eq. (F24) can be shown using Eq. (F28) and that, under the conditions given, $Z_{i\sigma}Z_{l\sigma'}$ commutes with $a_{j\sigma}$:

$$\{Z_{i\sigma}Z_{l\sigma'}, B_{ij\sigma}\} = -\tau\{Z_{i\sigma}Z_{l\sigma'}, a_{i\sigma}^\dagger a_{j\sigma}\} = -\tau\{Z_{i\sigma}Z_{l\sigma'}, a_{i\sigma}^\dagger\}a_{j\sigma} = 0. \quad (\text{F31})$$

Finally, Eq. (F24) is equivalent to Eq. (F25) by taking the Hermitian conjugate

$$\{Z_{i\sigma}Z_{l\sigma'}, B_{ij\sigma}\} = 0 \Leftrightarrow \{Z_{i\sigma}Z_{l\sigma'}, B_{ji\sigma}\} = 0. \quad (\text{F32})$$

We next proceed by deriving expressions for the two commutator bounds of interest.

3. Commutator bound $\|[[H_I + H_V, H_h], H_I + H_V]\|$

Here, we prove the first of two central commutator bounds.

Lemma F.1. *For an extended Hubbard model Hamiltonian $H_{EH} = H_h + H_I + H_V$, defined in Eqs. (F3)–(F5), on a lattice with N lattice sites where all sites have k nearest neighbors, then*

$$\|[[H_I + H_V, H_h], H_I + H_V]\| \leq (U^2 + V^2k)\|H_h\| + \left((4k - 2)UV\tau + (k - 1)(4k - 1)V^2\tau\right)kN. \quad (\text{F33})$$

Proof. Our first step is to evaluate the commutator $[H_I + H_V, B_{ij} + B_{ji}]$. In the following, we determine the Coulomb interaction terms that contain spin orbitals on lattice sites i and j , since all other Coulomb terms commute with B_{ij} and B_{ji} according to Eq. (F22). The Coulomb terms that contain spin orbitals on site i and j are

$$H_{C,ij} = \frac{U}{4}\left(Z_{i\uparrow}Z_{i\downarrow} + Z_{j\uparrow}Z_{j\downarrow}\right) + \frac{V}{4}\left(Z_{i\uparrow}Z_{j\uparrow} + Z_{i\uparrow}Z_{j\downarrow} + Z_{i\downarrow}Z_{j\uparrow} + Z_{i\downarrow}Z_{j\downarrow} + (Z_{i\uparrow} + Z_{i\downarrow})\Sigma^i + (Z_{j\uparrow} + Z_{j\downarrow})\Sigma^j\right), \quad (\text{F34})$$

where we use Σ^i as the sum over the Z -operators on the nearest neighbors of i other than site j , and similarly we use Σ^j as the sum over Z -operators on the nearest neighbors of j other than i . These operators are defined as

$$\Sigma^i \equiv \sum_{\sigma \in \{\uparrow, \downarrow\}} \sum_{l \sim i, l \neq j} Z_{l\sigma}, \quad \Sigma^j \equiv \sum_{\sigma \in \{\uparrow, \downarrow\}} \sum_{l \sim j, l \neq i} Z_{l\sigma}. \quad (\text{F35})$$

The operators Σ^i and Σ^j contain $2(k - 1)$ operators of type $Z_{l\sigma}$. Continuing, the sum over spins will be written as $\sum_{\sigma \in \{\uparrow, \downarrow\}} = \sum_{\sigma}$.

We proceed by evaluating the commutator $[H_I + H_V, B_{ij\sigma} + B_{ji\sigma}] = [H_{C,ij}, B_{ij\sigma} + B_{ji\sigma}]$ using the commutators and anti-commutators in Eqs. (F23)–(F25),

$$[H_{C,ij}, B_{ij\sigma} + B_{ji\sigma}] = \frac{V}{2} \left(V_{ij} + Z_{i\sigma} \Sigma^i + Z_{j\sigma} \Sigma^j \right) (B_{ij\sigma} + B_{ji\sigma}), \quad (\text{F36})$$

where $V_{ij} \equiv \frac{U}{V} Z_{i\uparrow} Z_{i\downarrow} + \frac{U}{V} Z_{j\uparrow} Z_{j\downarrow} + Z_{i\uparrow} Z_{j\downarrow} + Z_{i\downarrow} Z_{j\uparrow}$. The commutator in (F36) is nested with $H_I + H_V$. We use that the Coulomb terms commute to evaluate the nested commutator

$$\begin{aligned} [[H_I + H_V, B_{ij\sigma} + B_{ji\sigma}], H_I + H_V] &= \frac{V}{2} \left(V_{ij} + Z_{i\sigma} \Sigma^i + Z_{j\sigma} \Sigma^j \right) [B_{ij\sigma} + B_{ji\sigma}, H_I + H_V], \\ &= -\frac{V^2}{4} \left(V_{ij} + Z_{i\sigma} \Sigma^i + Z_{j\sigma} \Sigma^j \right)^2 (B_{ij\sigma} + B_{ji\sigma}). \end{aligned} \quad (\text{F37})$$

Then, we obtain $[[H_I + H_V, B_{ij} + B_{ji}], H_I + H_V]$ by summing over σ in Eq. (F37),

$$[[H_I + H_V, B_{ij} + B_{ji}], H_I + H_V] = -\frac{V^2}{4} \sum_{\sigma} \left(V_{ij} + Z_{i\sigma} \Sigma^i + Z_{j\sigma} \Sigma^j \right)^2 (B_{ij\sigma} + B_{ji\sigma}). \quad (\text{F38})$$

Next, we multiply the nested commutator by $\frac{1}{2}$ and sum over $\langle ij \rangle$ to obtain H_h (as in Eq. (F9)). We also expand the expression and define the two operators B_1 and $B_2^{i,j,\sigma}$,

$$\frac{1}{2} \sum_{\langle ij \rangle} [[H_I + H_V, B_{ij} + B_{ji}], H_I + H_V] = [[H_I + H_V, H_h], H_I + H_V] = B_1 + \sum_{\langle ij \rangle} \sum_{\sigma} B_2^{i,j,\sigma}, \quad (\text{F39})$$

$$B_1 = -\frac{V^2}{8} \sum_{\langle ij \rangle} \left(V_{ij}^2 + 4(k-1)\mathbb{1} \right) (B_{ij} + B_{ji}), \quad (\text{F40})$$

$$B_2^{i,j,\sigma} = -\frac{V^2}{4} \left(V_{ij} (Z_{i\sigma} \Sigma^i + Z_{j\sigma} \Sigma^j) + Z_{i\sigma} Z_{j\sigma} \Sigma^i \Sigma^j + \frac{1}{2} (G_{\neq}^i + G_{\neq}^j) \right) (B_{ij\sigma} + B_{ji\sigma}). \quad (\text{F41})$$

The B_1 term contains all Coulomb terms that only include interactions between spin orbitals on sites i and j , and the rest of the diagonal coming from squaring $Z_{i\sigma} \Sigma^i$ and $Z_{j\sigma} \Sigma^j$, using that $Z_{i\sigma}^2 = \mathbb{1}$ for any $i\sigma$. The $B_2^{i,j,\sigma}$ term contains all other interactions that are included in Eq. (F37). To simplify $B_2^{i,j,\sigma}$, we have introduced G_{\neq}^i and G_{\neq}^j that denotes all non-diagonal terms from $(Z_{i\sigma} \Sigma^i)^2$ and $(Z_{j\sigma} \Sigma^j)^2$, defined as $G_{\neq}^i \equiv (\Sigma^i)^2 - 2(k-1)\mathbb{1}$ and $G_{\neq}^j \equiv (\Sigma^j)^2 - 2(k-1)\mathbb{1}$.

We bound Eq. (F39) as

$$\| [[H_I + H_V, H_h], H_I + H_V] \| \leq \| B_1 \| + \sum_{\langle ij \rangle} \sum_{\sigma} \| B_2^{i,j,\sigma} \|. \quad (\text{F42})$$

We proceed by first evaluating $\| B_1 \|$ by expanding V_{ij}^2 ,

$$\begin{aligned} B_1 &= -\frac{V^2}{4} \sum_{\langle ij \rangle} \left(\frac{U^2}{V^2} \mathbb{1} + \mathbb{1} + \left(\frac{U^2}{V^2} + 1 \right) Z_{i\uparrow} Z_{i\downarrow} Z_{j\uparrow} Z_{j\downarrow} + 2 \frac{U}{V} (Z_{i\uparrow} Z_{j\uparrow} + Z_{i\downarrow} Z_{j\downarrow}) + 2(k-1)\mathbb{1} \right) (B_{ij} + B_{ji}), \\ &= -\frac{1}{4} \sum_{\langle ij \rangle} \left((U^2 + V^2(2k-1))(B_{ij} + B_{ji}) + (U^2 + V^2) Z_{i\uparrow} Z_{i\downarrow} Z_{j\uparrow} Z_{j\downarrow} (B_{ij} + B_{ji}) + 2UV (Z_{i\uparrow} Z_{j\uparrow} + Z_{i\downarrow} Z_{j\downarrow}) (B_{ij} + B_{ji}) \right). \end{aligned} \quad (\text{F43})$$

We employ a trick that uses the unitary operator \bar{V} , where $\bar{V} = \prod_k \frac{1}{\sqrt{2}} (\mathbb{1} + i Z_{k\uparrow} Z_{k\downarrow})$, to rewrite $Z_{i\uparrow} Z_{i\downarrow} Z_{j\uparrow} Z_{j\downarrow} B_{ij}$ as $-\bar{V} B_{ij} \bar{V}^\dagger$ for any i and j . This trick is defined and used in Eqs. (C10)–(C14) in Ref. [21]. This allows us to write

$$\sum_{\langle ij \rangle} Z_{i\uparrow} Z_{i\downarrow} Z_{j\uparrow} Z_{j\downarrow} (B_{ij} + B_{ji}) = \sum_{\langle ij \rangle} \left(-\bar{V} B_{ij} \bar{V}^\dagger - \bar{V} B_{ji} \bar{V}^\dagger \right) = -2\bar{V} H_h \bar{V}^\dagger. \quad (\text{F44})$$

We use this to write B_1 as

$$B_1 = -\frac{1}{2} (U^2 + V^2(2k-1)) H_h + \frac{1}{2} (U^2 + V^2) \bar{V} H_h \bar{V}^\dagger + \frac{1}{2} UV \sum_{\langle ij \rangle} (Z_{i\uparrow} Z_{j\uparrow} + Z_{i\downarrow} Z_{j\downarrow}) (B_{ij} + B_{ji}). \quad (\text{F45})$$

We take the norm of this expression and apply the triangle inequality. The expression is evaluated using unitary invariance of the norm, $\|\prod_{i\sigma} Z_{i\sigma}\| = 1$ and computing $\|B_{ij} + B_{ji}\| = 2\tau$ (to evaluate this, we refer to Section F 1 of this Appendix).

$$\|B_1\| \leq \frac{1}{2}(U^2 + V^2(2k-1))\|H_h\| + \frac{1}{2}(U^2 + V^2)\|H_h\| + UV \sum_{\langle ij \rangle} \|B_{ij} + B_{ji}\| = (U^2 + V^2k)\|H_h\| + 2UV\tau kN. \quad (\text{F46})$$

Next, we bound $\|B_2^{i,j,\sigma}\|$ by applying the triangle inequality and using $\|B_{ij\sigma} + B_{ji\sigma}\| = \tau$,

$$\|B_2^{i,j,\sigma}\| \leq \frac{V^2\tau}{4} \left(\|V_{ij}(Z_{i\sigma}\Sigma^i + Z_{j\sigma}\Sigma^j)\| + \|Z_{i\sigma}Z_{j\sigma}\Sigma^i\Sigma^j\| + \frac{1}{2}\|G_{\neq}^i + G_{\neq}^j\| \right), \quad (\text{F47})$$

and further bound each of the terms in the above expression using $\|\prod_{i,\sigma} Z_{i\sigma}\| = 1$,

$$\|V_{ij}(Z_{i\sigma}\Sigma^i + Z_{j\sigma}\Sigma^j)\| \leq 8\left(\frac{U}{V} + 1\right)(k-1), \quad (\text{F48})$$

$$\|Z_{i\sigma}Z_{j\sigma}\Sigma^i\Sigma^j\| \leq 4(k-1)^2, \quad (\text{F49})$$

$$\frac{1}{2}\|G_{\neq}^i + G_{\neq}^j\| \leq (2(k-1))^2 - 2(k-1) = (k-1)(4k-6). \quad (\text{F50})$$

These expressions are inserted back into Eq. (F47) and simplified

$$\|B_2^{i,j,\sigma}\| \leq \frac{V^2\tau}{4}(k-1) \left(8\left(\frac{U}{V} + 1\right) + 4(k-1) + 4k-6 \right) = \frac{\tau(k-1)}{2} (4UV + V^2(4k-1)). \quad (\text{F51})$$

Now, the expressions for $\|B_1\|$ and $\|B_2^{i,j,\sigma}\|$ are inserted back into Eq. (F42). Since the derived bound on $\|B_2^{i,j,\sigma}\|$ is independent of i, j and σ , we can replace the summation over these values by a factor of $2kN$, using that $\sum_{\langle ij \rangle}$ runs over kN nearest-neighbor terms and that \sum_{σ} runs over 2 spin values. Simplifying, we then obtain

$$\begin{aligned} \left\| [[H_I + H_V, H_h], H_I + H_V] \right\| &\leq (U^2 + V^2k)\|H_h\| + \left(2UV\tau + \tau(k-1)(4UV + V^2(4k-1)) \right) kN, \\ &= (U^2 + V^2k)\|H_h\| + \left((4k-2)UV\tau + (k-1)(4k-1)V^2\tau \right) kN, \end{aligned} \quad (\text{F52})$$

which proves Lemma F.1. \square

Furthermore, we present a corollary where this commutator bound is calculated for the periodic hexagonal lattice.

Corollary F.2. *For a periodic hexagonal lattice with N lattice sites where each site has $k = 3$ nearest neighbors, the commutator bound can be evaluated as*

$$\left\| [[H_I + H_V, H_h], H_I + H_V] \right\| \leq (\tau U^2 + 3\tau V^2)\|R\|_1 + (30UV\tau + 66V^2\tau)N \quad (\text{F53})$$

where R is the adjacency matrix of the periodic hexagonal lattice and $\|\cdot\|_1$ is the Schatten one-norm.

Proof. To show this, we simply use that $k = 3$ for the periodic hexagonal lattice and that the operator norm of H_h can be evaluated as $\|H_h\| = \tau\|R\|_1$ as shown in subsection F 1. \square

4. Commutator bound $\left\| [[H_V, H_h], H_h] \right\|$

We continue by evaluating an expression for the second central commutator bound. Note that the expressions apply for lattices where all lattice sites have k nearest neighbors.

First, we define $H_{k,\sigma}^i$ and $H_{k-1,\sigma}^{ij}$ as local hopping operators around the site i , where j is one of the neighbors, in spin sector σ as

$$H_{k,\sigma}^i = -\tau \sum_{mn} (\tilde{S}_k^i)_{mn} a_{m\sigma}^\dagger a_{n\sigma}, \quad H_{k-1,\sigma}^{ij} = -\tau \sum_{mn} (\tilde{S}_{k-1}^{ij})_{mn} a_{m\sigma}^\dagger a_{n\sigma}, \quad (\text{F54})$$

where we use m and n as the site indices in the sum to avoid confusion with the specific sites i and j . In $(\tilde{S}_k^i)_{mn}$ and $(\tilde{S}_{k-1}^{ij})_{mn}$, the subscript mn indicates a specific entry of the matrices \tilde{S}_k^i and \tilde{S}_{k-1}^{ij} .

In Eq. (F54), \tilde{S}_k^i is an $N \times N$ matrix whose only non-zero terms are a sub-block corresponding to an S_k star graph located at site i (as in the examples described in Eqs. (F18)–(F21)). Similarly, $\tilde{S}_{k-1,\sigma}^{ij}$ is an $N \times N$ matrix whose only non-zero terms are a sub-block corresponding to an S_{k-1} star graph located at site i , but where the hopping terms between the neighboring sites i and j are disregarded compared to \tilde{S}_k^i . For general lattices the norms of $H_{k,\sigma}^i$ and $H_{k,\sigma}^{ij}$ are in principle dependent on sites i and j , but we omit site dependency under the norm because we only consider lattices for which each site has the same number of nearest neighbors; in this case there is no dependence.

Lemma F.3. *For an extended Hubbard model Hamiltonian $H_{EH} = H_h + H_I + H_V$, defined in Eqs. (F3)–(F5), on a lattice with N lattice sites where all sites have k nearest neighbors, then*

$$\| [[H_V, H_h], H_h] \| \leq V k N \left(\| [H_{k-1,\sigma}, H_h] \| + 4 \| H_{k-1,\sigma} \|^2 + \| [H_{k,\sigma}, H_h] \| + 2 \| H_{k,\sigma} \|^2 \right), \quad (\text{F55})$$

where $H_{k-1,\sigma}^{ij}$ and $H_{k,\sigma}^i$ are defined in Eq. F54, and we drop the i and j superscripts as site dependence is removed under the norm.

Proof. First, we write the Coulomb interaction terms in the commutator $[[H_V, H_h], H_h]$ as a sum over lattice sites i . The sum over Coulomb terms on site j neighbor to site i is written as $\sum_{j \sim i} (Z_{j\uparrow} + Z_{j\downarrow})$, which means the commutator can be written as

$$[[H_V, H_h], H_h] = \frac{V}{8} \sum_i [(Z_{i\uparrow} + Z_{i\downarrow}) \sum_{j \sim i} (Z_{j\uparrow} + Z_{j\downarrow}), H_h], H_h]. \quad (\text{F56})$$

We wish to bound the norm of this commutator. Using the triangle inequality, we write

$$\| [[H_V, H_h], H_h] \| \leq \frac{V}{8} \sum_i \sum_{j \sim i} \| [(Z_{i\uparrow} + Z_{i\downarrow})(Z_{j\uparrow} + Z_{j\downarrow}), H_h], H_h] \|. \quad (\text{F57})$$

We proceed by evaluating the commutator $[(Z_{i\uparrow} + Z_{i\downarrow})(Z_{j\uparrow} + Z_{j\downarrow}), H_h]$ which contains two types of terms where the neighboring orbitals on sites i and j either have the same or opposite spin: $[Z_{i\sigma} Z_{j\sigma}, H_h]$ and $[Z_{i\sigma} Z_{j\bar{\sigma}}, H_h]$, where $\bar{\sigma}$ denotes the opposite spin of σ . We evaluate these commutators using the rules in Eqs. (F22)–(F25),

$$[Z_{i\sigma} Z_{j\sigma}, H_h] = 2Z_{i\sigma} Z_{j\sigma} \left(\sum_{l \sim i, l \neq j} (B_{il\sigma} + B_{li\sigma}) + \sum_{l \sim j, l \neq i} (B_{jl\sigma} + B_{lj\sigma}) \right), \quad (\text{F58})$$

$$[Z_{i\sigma} Z_{j\bar{\sigma}}, H_h] = 2Z_{i\sigma} Z_{j\bar{\sigma}} \left(\sum_{l \sim i} (B_{il\sigma} + B_{li\sigma}) + \sum_{l \sim j} (B_{jl\bar{\sigma}} + B_{lj\bar{\sigma}}) \right). \quad (\text{F59})$$

We note that these commutators contain expressions that correspond to the hopping operators $H_{k,\sigma}^i$ and $H_{k-1,\sigma}^{ij}$ defined in Eq. (F54),

$$H_{k,\sigma}^i = \sum_{l \sim i} (B_{il\sigma} + B_{li\sigma}), \quad H_{k-1,\sigma}^{ij} = \sum_{l \sim i, l \neq j} (B_{il\sigma} + B_{li\sigma}). \quad (\text{F60})$$

Using these operators, the expressions in Eqs. (F58) and (F59) can be rewritten as

$$[Z_{i\sigma} Z_{j\sigma}, H_h] = 2Z_{i\sigma} Z_{j\sigma} \left(H_{k-1,\sigma}^{ij} + H_{k-1,\sigma}^{ji} \right), \quad (\text{F61})$$

$$[Z_{i\sigma} Z_{j\bar{\sigma}}, H_h] = 2Z_{i\sigma} Z_{j\bar{\sigma}} \left(H_{k,\sigma}^i + H_{k,\bar{\sigma}}^j \right). \quad (\text{F62})$$

These commutators are nested with H_h and evaluated using the commutator identity $[AB, C] = A[B, C] + [A, C]B$,

$$[[Z_{i\sigma} Z_{j\sigma}, H_h], H_h] = 2Z_{i\sigma} Z_{j\sigma} [H_{k-1,\sigma}^{ij} + H_{k-1,\sigma}^{ji}, H_h] + 2[Z_{i\sigma} Z_{j\sigma}, H_h] (H_{k-1,\sigma}^{ij} + H_{k-1,\sigma}^{ji}), \quad (\text{F63})$$

$$[[Z_{i\sigma} Z_{j\bar{\sigma}}, H_h], H_h] = 2Z_{i\sigma} Z_{j\bar{\sigma}} [H_{k,\sigma}^i + H_{k,\bar{\sigma}}^j, H_h] + 2[Z_{i\sigma} Z_{j\bar{\sigma}}, H_h] (H_{k,\sigma}^i + H_{k,\bar{\sigma}}^j). \quad (\text{F64})$$

Using Eqs. (F61) and (F62), these expressions can be simplified to

$$[[Z_{i\sigma} Z_{j\sigma}, H_h], H_h] = 2Z_{i\sigma} Z_{j\sigma} [H_{k-1,\sigma}^{ij} + H_{k-1,\sigma}^{ji}, H_h] + 4Z_{i\sigma} Z_{j\sigma} (H_{k-1,\sigma}^{ij} + H_{k-1,\sigma}^{ji})^2, \quad (\text{F65})$$

$$[[Z_{i\sigma} Z_{j\bar{\sigma}}, H_h], H_h] = 2Z_{i\sigma} Z_{j\bar{\sigma}} [H_{k,\sigma}^i + H_{k,\bar{\sigma}}^j, H_h] + 4Z_{i\sigma} Z_{j\bar{\sigma}} (H_{k,\sigma}^i + H_{k,\bar{\sigma}}^j)^2. \quad (\text{F66})$$

We take the operator norm of these expressions and use the triangle inequality. We also use $\|AB\| \leq \|A\| \cdot \|B\|$ and $\|Z_{i\sigma}Z_{j\sigma'}\| = 1$ for all i, j, σ and σ' to obtain

$$\|[[Z_{i\sigma}Z_{j\sigma}, H_h], H_h]\| \leq 2\|[H_{k-1,\sigma}^{ij} + H_{k-1,\sigma}^{ji}, H_h]\| + 4\|(H_{k-1,\sigma}^{ij} + H_{k-1,\sigma}^{ji})^2\|, \quad (\text{F67})$$

$$\|[[Z_{i\sigma}Z_{j\bar{\sigma}}, H_h], H_h]\| \leq 2\|[H_{k,\sigma}^i + H_{k,\bar{\sigma}}^j, H_h]\| + 4\|(H_{k,\sigma}^i + H_{k,\bar{\sigma}}^j)^2\|. \quad (\text{F68})$$

We use the triangle inequality to split the norm of the commutators

$$\|[[Z_{i\sigma}Z_{j\sigma}, H_h], H_h]\| \leq 2(\|[H_{k-1,\sigma}^{ij}, H_h]\| + \|[H_{k-1,\sigma}^{ji}, H_h]\|) + 4\|(H_{k-1,\sigma}^{ij} + H_{k-1,\sigma}^{ji})^2\|, \quad (\text{F69})$$

$$\|[[Z_{i\sigma}Z_{j\bar{\sigma}}, H_h], H_h]\| \leq 2(\|[H_{k,\sigma}^i, H_h]\| + \|[H_{k,\bar{\sigma}}^j, H_h]\|) + 4\|(H_{k,\sigma}^i + H_{k,\bar{\sigma}}^j)^2\|, \quad (\text{F70})$$

Next, we write the norms of the squares as

$$\|(H_{k-1,\sigma}^{ij} + H_{k-1,\sigma}^{ji})^2\| = \|(H_{k-1,\sigma}^{ij})^2 + (H_{k-1,\sigma}^{ji})^2 + H_{k-1,\sigma}^{ij}H_{k-1,\sigma}^{ji} + H_{k-1,\sigma}^{ji}H_{k-1,\sigma}^{ij}\|, \quad (\text{F71})$$

$$\|(H_{k,\sigma}^i + H_{k,\bar{\sigma}}^j)^2\| = \|(H_{k,\sigma}^i)^2 + (H_{k,\bar{\sigma}}^j)^2\|, \quad (\text{F72})$$

using that $H_{k,\sigma}^i$ and $H_{k,\bar{\sigma}}^j$ are block diagonal because they act in different spin sectors to remove the cross terms. We bound the norms in Eqs. (F71) and (F72) using the triangle inequality and $\|AB\| \leq \|A\| \cdot \|B\|$,

$$\|(H_{k-1,\sigma}^{ij} + H_{k-1,\sigma}^{ji})^2\| \leq \|H_{k-1,\sigma}^{ij}\|^2 + \|H_{k-1,\sigma}^{ji}\|^2 + \|H_{k-1,\sigma}^{ij}\| \|H_{k-1,\sigma}^{ji}\| + \|H_{k-1,\sigma}^{ji}\| \|H_{k-1,\sigma}^{ij}\|, \quad (\text{F73})$$

$$\|(H_{k,\sigma}^i + H_{k,\bar{\sigma}}^j)^2\| \leq \|H_{k,\sigma}^i\|^2 + \|H_{k,\bar{\sigma}}^j\|^2. \quad (\text{F74})$$

We note that the norm of the operators $H_{k-1,\sigma}^{ij}$ and $H_{k,\sigma}^i$ are independent of the specific sites i and j because each site has the same number of nearest neighbors. We therefore drop these superscripts in the following step. We also replace $\bar{\sigma}$ by σ because the norm is independent of which spin sector we use. This allows us to write Eqs. (F69) and (F70) as

$$\|[[Z_{i\sigma}Z_{j\sigma}, H_h], H_h]\| \leq 4\|[H_{k-1,\sigma}, H_h]\| + 16\|H_{k-1,\sigma}\|^2, \quad (\text{F75})$$

$$\|[[Z_{i\sigma}Z_{j\bar{\sigma}}, H_h], H_h]\| \leq 4\|[H_{k,\sigma}, H_h]\| + 8\|H_{k,\sigma}\|^2. \quad (\text{F76})$$

These expressions are inserted back into Eq. (F57) which, for each (i, j) pair, contains two terms where the spin orbitals on sites i and j have same spin, as in Eq. (F75), and two terms where the spin orbitals on sites i and j have opposite spins, as in Eq. (F76). Because the resulting bound on the norm inside the summation is independent of i and j , we can also simply replace the summation over i and j by a factor of kN . This yields the expression

$$\|[[H_V, H_h], H_h]\| \leq V k N \left(\|[H_{k-1,\sigma}, H_h]\| + 4\|H_{k-1,\sigma}\|^2 + \|[H_{k,\sigma}, H_h]\| + 2\|H_{k,\sigma}\|^2 \right), \quad (\text{F77})$$

which concludes the proof of Lemma F.3. \square

Corollary F.4. *For a periodic hexagonal lattice with N lattice sites where all sites have $k = 3$ nearest neighbors the following bound can be obtained*

$$\|[[H_V, H_h], H_h]\| \leq 3V\tau^2 N(16 + 2\sqrt{3}). \quad (\text{F78})$$

Proof. For the hexagonal lattice, the commutator bound $\|[[H_V, H_h], H_h]\|$ can be evaluated as

$$\|[[H_V, H_h], H_h]\| \leq 3VN \left(\|[H_{2,\sigma}, H_h]\| + 4\|H_{2,\sigma}\|^2 + \|[H_{3,\sigma}, H_h]\| + 2\|H_{3,\sigma}\|^2 \right), \quad (\text{F79})$$

using $k = 3$. These operator norms can be evaluated following the strategy outlined in F 1 in Eqs. (F20)–(F21).

The norms are evaluated as

$$\|[H_{2,\sigma}, H_h]\| = \frac{\tau^2}{2} \|\tilde{S}_2, R\|_1 = 2\sqrt{3}\tau^2, \quad (\text{F80})$$

$$\|H_{2,\sigma}\| = \frac{\tau}{2} \|\tilde{S}_2\|_1 = \sqrt{2}\tau, \quad (\text{F81})$$

$$\|[H_{3,\sigma}, H_h]\| = \frac{\tau^2}{2} \|\tilde{S}_3, R\|_1 = \sqrt{6}\tau^2, \quad (\text{F82})$$

$$\|H_{3,\sigma}\| = \frac{\tau}{2} \|\tilde{S}_3\|_1 = \sqrt{3}\tau, \quad (\text{F83})$$

TABLE II. Tile Trotterization error norms (W_{tile}), qubit counts (N_Q), arbitrary rotation costs (N_R) and T gate costs (N_T) for performing a single Trotter step for periodic hexagonal lattice Hubbard models with lattice parameters $L_x = L_y = L$, where $4 \leq L \leq 18$ for even L , and Hubbard model parameters $U = 4$, $V = 2$ and $\tau = 1$. The Hubbard model parameters only affects the Trotter error norms. We show data for the resources required to implement Tile Trotterization for the periodic Hubbard model and the periodic extended Hubbard model without HWP ($\alpha = 0$) and with HWP using $\alpha = N/4 - 1$, $\alpha = N/2 - 1$ and $\alpha = N - 1$ ancilla qubits. The data from this table can be used to reproduce the Tile Trotterization costings shown in Figs. 2 and 3.

	$N = 2L^2$	32	72	128	200	288	392	512	648
Hubbard model	W_{tile}	215	483	860	1344	1934	2634	3439	4353
Extended Hubbard model	W_{tile}	1223	2752	4894	7648	11011	14989	19577	24778
Hubbard model, $\alpha = 0$	N_Q	64	144	256	400	576	784	1024	1296
	N_R	192	432	768	1200	1728	2352	3072	3888
	N_T	320	720	1280	2000	2880	3920	5120	6480
Hubbard model, $\alpha = \frac{N}{4} - 1$	N_Q	71	161	287	449	647	881	1151	1457
	N_R	96	120	144	144	168	168	192	192
	N_T	992	2352	4256	6704	9696	13232	17312	21936
Hubbard model, $\alpha = \frac{N}{2} - 1$	N_Q	79	179	319	499	719	979	1279	1619
	N_R	60	72	84	84	96	96	108	108
	N_T	1040	2400	4304	6752	9744	13280	17360	21984
Hubbard model, $\alpha = N - 1$	N_Q	95	215	383	599	863	1175	1535	1943
	N_R	36	42	48	48	54	54	60	60
	N_T	1064	2424	4328	6776	9768	13304	17384	22008
Extended Hubbard model, $\alpha = 0$	N_Q	64	144	256	400	576	784	1024	1296
	N_R	384	864	1536	2400	3456	4704	6144	7776
	N_T	320	720	1280	2000	2880	3920	5120	6480
Extended Hubbard model, $\alpha = \frac{N}{4} - 1$	N_Q	71	161	287	449	647	881	1151	1457
	N_R	192	240	288	288	336	336	384	384
	N_T	1664	3984	7232	11408	16512	22544	29504	37392
Extended Hubbard model, $\alpha = \frac{N}{2} - 1$	N_Q	79	179	319	499	719	979	1279	1619
	N_R	120	144	168	168	192	192	216	216
	N_T	1760	4080	7328	11504	16608	22640	29600	37488
Extended Hubbard model, $\alpha = N - 1$	N_Q	95	215	383	599	863	1175	1535	1943
	N_R	72	84	96	96	108	108	120	120
	N_T	1808	4128	7376	11552	16656	22688	29648	37536

where R is the adjacency matrix of a periodic hexagonal lattice. We used a periodic hexagonal lattice model with $L_x = L_y = 4$ to numerically obtain Eqs. (F80) and (F82), which are independent of the lattice size beyond a small value of L . We insert these norms back into Eq. (F77) and obtain

$$\|[[H_V, H_h], H_h]\| \leq 3V\tau^2 N(2\sqrt{3} + 8 + 2 + 6) = 3V\tau^2 N(16 + 2\sqrt{3}), \quad (\text{F84})$$

which concludes the proof of Corollary F.4. \square

Appendix G: Tile Trotterization Error Norms and Resource Requirements

In Table II we provide the Tile Trotterization error norms (W_{tile}), the total number of qubits (N_Q), and the number of arbitrary rotations (N_R) and T gates (N_T) required per Trotter step for the hexagonal lattice Hubbard model simulations considered in Figs. 2 and 3. We use Hubbard model parameters $U = 4$, $V = 2$ and $\tau = 1$. The nearest-neighbor interaction parameter, V , is only used in the extended Hubbard model. All systems use the periodic hexagonal lattice model described in Appendix D with parameters $L_x = L_y = L$ and $4 \leq L \leq 18$, for even L .

Appendix H: Qubitization circuits

In this section we describe how qubitization circuits may be implemented for the Hubbard model on a periodic hexagonal lattice. Our qubitization approach builds upon previous work by Babbush *et al.* in Ref. [40]. In Section VI we compared the cost of QPE performed with both Tile Trotterization and qubitization-based approaches. Here, we

provide a brief introduction to the qubitization approach, and present the implementations and costing of SELECT and PREPARE operators used for our QPE resource estimates.

In Trotter-based QPE, we perform phase estimation with a Trotterized approximation of the time evolution operator, $U = e^{-iHt}$. QPE allows us to estimate the eigenphases of this unitary, and therefore the energies of H . However, it is equally possible to perform phase estimation with other unitaries that encode the Hamiltonian. In qubitization, the unitary of interest is the walk operator, \mathcal{W} , which has eigenvalues

$$e^{\pm i \arccos(E_n/\lambda)}, \quad (\text{H1})$$

where E_n are the eigenvalues of H and λ is the L1 norm of H . From these, we can obtain estimates of energies, E_n .

The quantum walk operator is built from SELECT and PREPARE operators. Consider a Hamiltonian

$$H = \sum_{l=0}^{L-1} w_l P_l, \quad \lambda = \sum_{l=0}^{L-1} |w_l|, \quad (\text{H2})$$

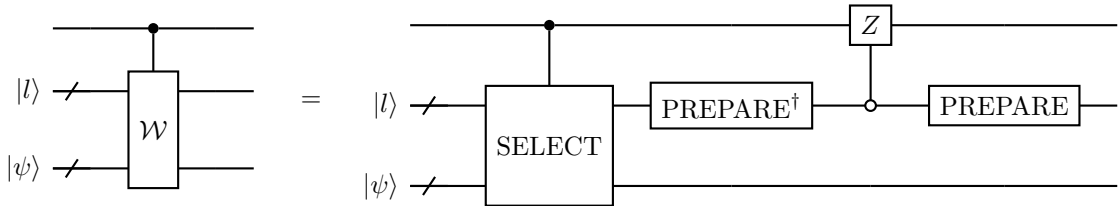
where $w_l > 0$ are coefficients and P_l are (tensor products of) Pauli operators. Then, SELECT defines a block-encoding of H/λ . In particular,

$$\text{SELECT} = \sum_{l=0}^{L-1} |l\rangle\langle l| \otimes P_l, \quad (\text{H3})$$

where $|l\rangle$ are flag qubit states. Each state $|l\rangle$ flags a corresponding term in the Hamiltonian, P_l . The PREPARE operator acts on the $|0\rangle$ state of the flag qubits and prepares a state that encodes the coefficients of H . More formally, it prepares the signal state that flags the block encoding of H/λ . It can be defined by

$$\text{PREPARE}|0\rangle = \sum_{l=0}^{L-1} \sqrt{\frac{w_l}{\lambda}} |l\rangle. \quad (\text{H4})$$

The walk operator can be expressed in terms of the SELECT and PREPARE operations, and a reflection operator. In particular, it has been shown that the walk operator controlled on a single ancilla qubit can be expressed by the following operations:



Below we will describe the implementation and costing of each of these operations.

We will consider the following form of the Hubbard Hamiltonian, where the Jordan-Wigner mapping and a chemical potential shift are applied,

$$H_H^{\text{JW}} = -\frac{\tau}{2} \sum_{\langle p,q \rangle, \sigma} \left(X_{p\sigma} \vec{Z} X_{q\sigma} + Y_{p\sigma} \vec{Z} Y_{q\sigma} \right) + \frac{U}{4} \sum_{p=1}^N Z_{p\uparrow} Z_{p\downarrow}, \quad (\text{H5})$$

where X , Y and Z are Pauli operators. We label the Hamiltonian by JW and relabel the site indices as p and q in order to distinguish from the fermionic Hamiltonians defined in Section II. The operators \vec{Z} indicate a string of Z operators acting on all qubits between $p\sigma$ and $q\sigma$ in the JW ordering.

The gate cost of qubitization-based QPE scales with the L1 norm of the Hamiltonian. For the Hubbard model Hamiltonian, the L1 norm, λ , is given by

$$\lambda = 2\tau \times \# \text{ of bonds} + \frac{U}{4} \times \# \text{ of sites}. \quad (\text{H6})$$

The number of sites is N and for the periodic hexagonal lattice the number of bonds is $3N/2$, and therefore,

$$\lambda = \left(3\tau + \frac{U}{4} \right) N. \quad (\text{H7})$$

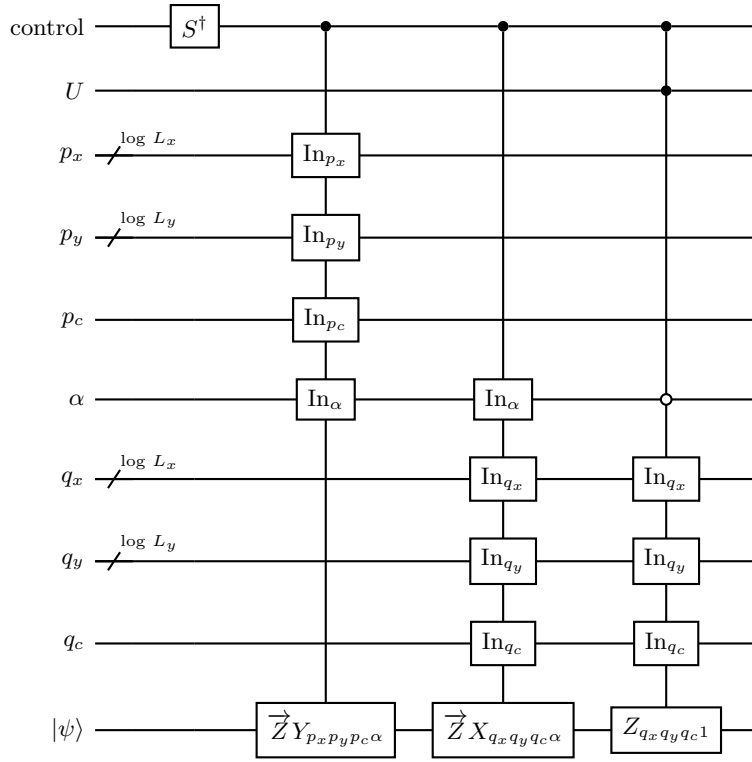


FIG. 9. Controlled SELECT circuit for the Hubbard model on an $L_x \times L_y$ periodic hexagonal lattice.

1. SELECT

We first consider the implementation of SELECT for the Hubbard model on a periodic hexagonal lattice. We index terms in the Hamiltonian using the flag registers $|U\rangle |p_x\rangle |p_y\rangle |p_c\rangle |\alpha\rangle |q_x\rangle |q_y\rangle |q_c\rangle$. We then define the action of SELECT as

$$\text{SELECT}|U, p, \alpha, q\rangle |\psi\rangle = |U, p, \alpha, q\rangle \begin{cases} Z_{p_0} Z_{q_1} |\psi\rangle & U \wedge (p = q) \wedge (\alpha = 0) \\ -X_{p\alpha} \vec{Z} X_{q\alpha} |\psi\rangle & \neg U \wedge (p < q) \\ -Y_{q\alpha} \vec{Z} Y_{p\alpha} |\psi\rangle & \neg U \wedge (p > q) \\ \text{UNDEFINED} & \text{otherwise.} \end{cases}$$

The labels p and q are lattice site indices that also include the “color” label, c , coming from the white and grey labels of the lattice points in each (l_x, l_y) pair, as shown in Fig. 6(a). We define the ordering $p = p_x + p_y L_y + p_c L_x L_y$ and $q = q_x + q_y L_y + q_c L_x L_y$. Note that all $c = 0$ terms come before all $c = 1$ terms within this ordering. Also note that for use in qubitized QPE, the action of the UNDEFINED block must be such that the total action of SELECT is Hermitian.

The quantum circuit to achieve this definition of SELECT, controlled on an ancilla qubit, is presented in Fig. 9, and consists of three unary iterators. The Toffoli cost of the first two unary iterators are $4L_x L_y - 1$ each, while the Toffoli cost of the final iterator, which has two additional controls, is $(2L_x L_y - 1) + 2 = 2L_x L_y + 1$, and so the total Toffoli cost combined is $10L_x L_y - 1$. This leads to a T gate cost of $C_S = 40L_x L_y - 4$. Expressing this in terms of the number of lattice points, N , we obtain $C_S = 20N - 4$. This is asymptotically the most expensive subroutine in the walk operator.

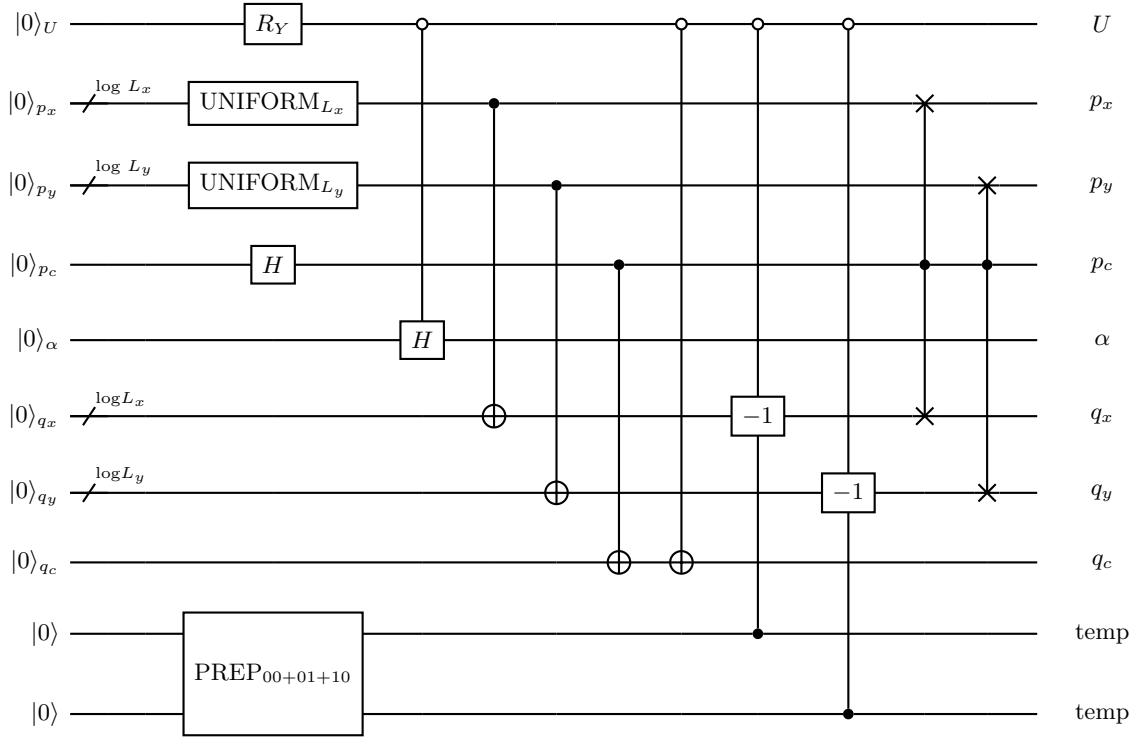


FIG. 10. PREPARE circuit for the Hubbard model on an $L_x \times L_y$ hexagonal lattice. Note that the controlled “ -1 ” operations on the $|q_x\rangle$ and $|q_y\rangle$ registers can be performed mod $2^{\lceil \log_2 L_x \rceil}$ and mod $2^{\lceil \log_2 L_y \rceil}$, respectively. They do not need to be performed mod L_x and mod L_y , as one might expect. This is discussed further in the text of Appendix H.

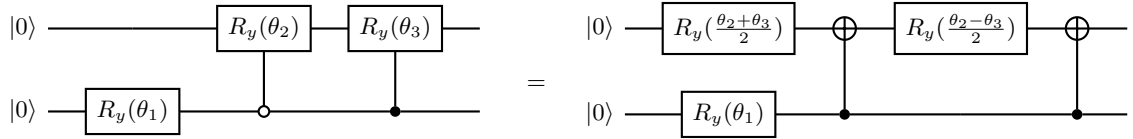


FIG. 11. Demonstration of how $\text{PREP}_{00+01+10}$ can be implemented. This requires 3 rotation gates, which can be implemented to precision ϵ with an expected T gate count of $1.15 \log(\frac{1}{\epsilon}) + 9.2$ each. In the text, we denote the number of T gates used to implement each of these rotations by Γ , which we set to 40.

2. PREPARE

The action of PREPARE is defined to act on the flag qubits prepared in state $|0\rangle$ as

$$\begin{aligned}
 \text{PREPARE } |0\rangle &= \sqrt{\frac{U}{4\lambda}} \sum_{p_x=0}^{L_x-1} \sum_{p_y=0}^{L_y-1} \sum_{p_c=0}^1 |1\rangle_U |p_x, p_y, p_c, 0\rangle |p_x, p_y, p_c\rangle \\
 &+ \sqrt{\frac{t}{2\lambda}} \sum_{p_x=0}^{L_x-1} \sum_{p_y=0}^{L_y-1} \sum_{\sigma=0}^1 |0\rangle_U \left(|p_x, p_y, 0, \sigma\rangle |p_x, p_y, 1\rangle + |p_x, p_y, 1, \sigma\rangle |p_x, p_y, 0\rangle \right. \\
 &\quad + |p_x, p_y, 0, \sigma\rangle |p_x - 1, p_y, 1\rangle + |p_x - 1, p_y, 1, \sigma\rangle |p_x, p_y, 0\rangle \\
 &\quad \left. + |p_x, p_y, 0, \sigma\rangle |p_x, p_y - 1, 1\rangle + |p_x, p_y - 1, 1, \sigma\rangle |p_x, p_y, 0\rangle \right). \tag{H8}
 \end{aligned}$$

The quantum circuit to achieve this definition of PREPARE is shown in Fig. 10. This consists of a number of circuit elements that we will briefly explain. The final Toffoli and T gate costs and ancilla costs for each circuit element are

Circuit element	Toffoli count	T count (incl. Toffolis)	Ancilla qubits
Controlled SELECT	$10L_xL_y - 1$	$40L_xL_y - 4$	$\lceil \log_2 L_x \rceil + \lceil \log_2 L_y \rceil + 3$
PREPARE:			
UNIFORM $\frac{1}{\sqrt{L_x}} \sum_{l=0}^{L_x-1} l\rangle$	$3\lceil \log_2 L_x \rceil - 3\eta_{L_x} - 3$	$4 \times \text{Toffoli count} + 2\Theta$	$\lceil \log_2 L_x \rceil - \eta_{L_x} + 2$
UNIFORM $\frac{1}{\sqrt{L_y}} \sum_{l=0}^{L_y-1} l\rangle$	$3\lceil \log_2 L_y \rceil - 3\eta_{L_y} - 3$	$4 \times \text{Toffoli count} + 2\Theta$	$\lceil \log_2 L_y \rceil - \eta_{L_y} + 2$
concat. success qubits	1	4	1
controlled Hadamard	1	4	2
controlled -1 on q_x register	$\lceil \log_2 L_x \rceil$	$4\lceil \log_2 L_x \rceil$	$\lceil \log_2 L_x \rceil$
controlled -1 on q_y register	$\lceil \log_2 L_y \rceil$	$4\lceil \log_2 L_y \rceil$	$\lceil \log_2 L_y \rceil$
Two controlled swaps	$\lceil \log_2 L_x \rceil + \lceil \log_2 L_y \rceil$	$7\lceil \log_2 L_x \rceil + 7\lceil \log_2 L_y \rceil$	0
$R_Y(\theta)$	-	Γ	1
PREP ₀₀₊₀₁₊₁₀	-	3Γ	1
Reflection	$2(2\lceil \log_2 L_x \rceil + 2\lceil \log_2 L_y \rceil + 10) - 3$	$4 \times \text{Toffoli count}$	1

TABLE III. The cost of various circuit elements to perform the controlled quantized walk operator for the Hubbard model on the $L_x \times L_y$ periodic hexagonal Hubbard model. The T gate counts include the cost of converting Toffoli gates into T gates. The ‘‘ancilla qubits’’ column is the total number of ancilla qubits for each circuit element, without reusing qubits, and not including flag qubits. The value η_{L_x} (η_{L_y}) is the largest power of 2 that is a factor of L_x (L_y), Θ is the number of T gates per rotation in the UNIFORM state preparation circuits, and Γ is the number of T gates used to implement each of the other rotation gates in PREPARE. The ‘‘concat. success qubits’’ element refers to concatenating the success qubits from the two UNIFORM operations, which SELECT must be controlled on. The ‘‘reflection’’ step uses the result from [63] to perform a Z gate with n controls in $2n - 3$ Toffolis, with a single ancilla. In practice, ancilla qubits can mostly be shared between subroutines. The only ancillas that are not reused are: the rotation qubit and success flag qubit from each UNIFORM state preparation, the concatenated success qubit, and a qubit prepared in the $|T\rangle$ state in the controlled Hadamard operation. Otherwise, subroutines in PREPARE can use the $\lceil \log_2 L_x \rceil + \lceil \log_2 L_y \rceil + 3$ ancillas required by SELECT. Therefore, the total number of ancilla qubits required is $\lceil \log_2 L_x \rceil + \lceil \log_2 L_y \rceil + 9$, in addition to $2\lceil \log_2 L_x \rceil + 2\lceil \log_2 L_y \rceil + 6$ flag qubits.

summarized in Table III.

The UNIFORM operations perform uniform state preparation, and can be implemented using amplitude amplification by the approach described in Appendix A of Ref. [6]. However, we make a slight modification to the approach described there. In particular, Ref. [6] implements the ancilla rotation by using a phase-gradient ancilla register, which requires b_n ancilla qubits and $b_n - 3$ Toffoli gates. However, as noted in Appendix A of Ref. [77], when the rotation angle β is known classically, as is the case here, this can also be implemented efficiently using rotation synthesis. Here, we use this alternative approach, requiring just a single ancilla for the rotation synthesis. For this gadget, the rotation synthesis can be lower precision than elsewhere; we define Θ to be the number of T gates used for each rotation in each UNIFORM state preparation, which is separate from the number of T gates used in synthesis of other rotations in PREPARE, which we denote Γ . As described in [6], the Toffoli cost consists of two inequality tests and a reflection. Of the ancillas required, the rotation qubit and success flag qubit and cannot be reused by other routines. We also note that the walk operator’s reflection is controlled on the rotation and success qubits, which are included in the final Toffoli count.

The circuit to perform a controlled Hadamard gate is shown in Fig. 17 of the same paper by Lee *et al.* [6], which requires two ancilla qubits and one Toffoli gate. One of the ancilla qubits is prepared in a $|T\rangle$ state, which we choose to preserve for future applications of the walk operator; therefore, this ancilla qubit cannot be reused, which is accounted for in the total qubit count.

It is also necessary to prepare the state

$$|\Psi_{00+01+10}\rangle = \frac{1}{\sqrt{3}}(|00\rangle + |01\rangle + |10\rangle), \quad (\text{H9})$$

which we achieve using a circuit of the form in Fig. 11, using 3 rotation gates. We denote the number of T gates per rotation in this subroutine as Γ . For our costing in Section VI, we set $\Gamma = 40$.

We next consider how to perform the controlled ‘‘-1’’ operation. One might expect that we actually have to perform ‘‘ $-1 \bmod L_x$ ’’ or ‘‘ $-1 \bmod L_y$ ’’ operations to properly enforce periodic boundary conditions, similarly to the PREPARE circuit of Ref. [40]. However, we can avoid this complication. To see this, consider the case of an $L \times L$ periodic lattice, and let us consider the ‘‘-1’’ operation on the $|q_x\rangle$ register. This register will consist of $n = \lceil \log_2 L \rceil$ qubits. Before this operation, the register will hold a uniform superposition of states $|l\rangle$, for $0 \leq l \leq L - 1$. For $l \geq 1$ the ‘‘-1’’ operation will act in the expected manner. For $l = 0$ it will instead give the state $|2^n - 1\rangle$. By periodic boundary conditions, we need lattice sites with $x = 0$ to be connected to sites with $x = L - 1$, and so this may seem incorrect. However, provided that SELECT is implemented appropriately, this ultimately leads to the correct circuit.

In particular, the SELECT circuit consists of unary iterators which are designed to act on $|l\rangle$ for $l \leq L$. The action of a controlled unary iterator on $|l\rangle|\Psi\rangle$ is

$$|c\rangle|l\rangle|\Psi\rangle \rightarrow |c\rangle|l\rangle(P_l)^c|\Psi\rangle, \quad (\text{H10})$$

where $|c\rangle$ is the control qubit. In Ref. [40], the authors introduce optimizations to the basic SELECT circuit. This is achieved by removing “runs” of the OFF controls on the right side of the circuit. These result in the well-established “sawtooth” circuits, which can be implemented in $L - 1$ Toffoli gates. However, removing these OFF controls also allows us to simplify our circuits as described above. In particular, in this case it can be seen that

$$|c\rangle|2^n - 1\rangle|\Psi\rangle \rightarrow |c\rangle|2^n - 1\rangle(P_{L-1})^c|\Psi\rangle. \quad (\text{H11})$$

In words, if the value $l = 2^n - 1$ is provided to the unary iterator, it is guaranteed to select the $l = L - 1$ term, which is the desired behavior to enforce periodic boundary conditions. This is a convenient benefit of the optimized iterators, which avoids us needing to perform modular “ $-1 \bmod L$ ” addition, and instead allows us to simply perform “ $-1 \bmod 2^n$ ” addition.

The adder circuit can be further simplified, due to the fact that it always subtracts 1. For an n -bit binary number, subtracting 1 is equivalent to adding $1_1 1_2 \dots 1_n$. Therefore each bit of the value added is 1, and we can prepare and unprepare a single ancilla qubit by using two Toffoli gates to incorporate the two controls for the adders. Then we use the circuit from Ref. [77] (Fig. 18) to perform addition with respect to this ancilla, the Toffoli cost of which is $\lceil \log_2 L \rceil - 2$. Therefore, the total Toffoli costs of the two controlled adders are $\lceil \log_2 L_x \rceil$ and $\lceil \log_2 L_y \rceil$.
